Advanced Composites and Hybrid Materials (2025) 8:410
https://doi.org/10.1007/s42114-025-01469-w

REVIEW

Design strategies in developing MXene-based anti-icing/deicing coatings: toward energy-efficient and durable solutions

Amina Ben Ayed[1] · **Mina Namvari**[1]

Received: 16 May 2025 / Revised: 15 August 2025 / Accepted: 11 September 2025
© The Author(s) 2025

Abstract
MXene-based coatings have emerged as highly efficient materials for anti-icing and deicing applications, offering a combination of photo- and electrothermal properties. These coatings leverage high electrical conductivity, localized surface plasmon resonance (LSPR), and thermal stability of MXenes, particularly $Ti_3C_2T_x$, to achieve rapid ice melting and delayed freezing. Photo- and electrothermal coatings, which utilize solar energy and electric power, respectively, exhibit high efficiency in active deicing. Hybrid designs integrate superhydrophobicity, reducing heat transfer at the ice-coating interface and preventing secondary freezing. Functional modifications, such as hybridization with Ag nanowires (AgNWs), carbon nanotubes (CNTs), graphene oxide (GO), polydopamine (PDA), and polydimethylsiloxane (PDMS), further enhance conductivity, mechanical stability, and oxidation resistance. In this review, we explore the latest advancements in MXene-based anti-icing/deicing strategies, categorizing them into photothermal, electrothermal, and hybrid mechanisms. Despite these advancements, challenges remain in the scalability, long-term durability, and oxidation resistance of MXenes under real-world conditions. In the conclusion section, this review also highlights potential solutions, including surface modifications, polymer encapsulation, and self-healing composites, the importance of AI-driven material design, and self-powered deicing systems.

Keywords MXene · Anti-icing · Deicing · Superhydrophobic · Photothermal · Electrothermal · Joule heating · Energy-efficient coatings

1 Introduction

Icing is a natural and inevitable occurrence that, if left unaddressed, can significantly impact the performance and safety of various structures, including ships [1], power lines [2], aircraft [3], wind turbines [4], roads [5], buildings [6], and photovoltaic systems [7]. Ice accumulation has led to severe disasters, causing substantial economic losses and numerous fatalities. For example, a major ice storm in 2008 crippled power transmission networks across southern China, leading to an estimated €5 billion in reconstruction costs [8]. Similarly, ice accretion on wind turbines, a key component of renewable energy, led to a catastrophic collapse of a wind turbine in Wisconsin in 2023, destroying a major asset long before its expected lifespan [9]. In aviation, ice accumulation on engines and sensors has been a contributing factor in numerous fatal crashes, including those of Air Algérie Flight 5017 (2014), Bek Air Flight 2100 (2019), and Aero Caribbean Flight 883 (2010), demonstrating the high-stake nature of this challenge.

Historically, managing ice has relied on active deicing methods such as mechanical removal, thermal heating, and chemical spraying [9, 10]. While effective, these approaches are often inefficient, energy-intensive, and can cause significant environmental harm, making them unsustainable for widespread, long-term application. The limitations of these traditional methods have driven extensive research into passive anti-icing strategies, which aim to prevent ice formation or facilitate its removal without external energy input. This market for ice protection systems is substantial and growing, estimated to be worth €1.8 million by 2027 [11]. A key strategy for passive anti-icing involves materials that possess one or more of three characteristics: repelling water

✉ Mina Namvari
mina.namvari@sabanciuniv.edu

Amina Ben Ayed
amina.benayed@sabanciuniv.edu

[1] Sabanci University Nanotechnology Research and Application Center (SUNUM), Sabanci University, Tuzla 34956, Istanbul, Turkey

Published online: 05 November 2025

droplets, inhibiting ice nucleation, or reducing ice adhesion strength [12].

Superhydrophobic surfaces (SHSs) have shown promise by creating a thermal barrier that delays freezing of supercooled droplets through the Cassie-Baxter model [12]. Given that some ice formation is inevitable under persistent subzero conditions, a more pragmatic approach for durable anti-icing is to focus on minimizing ice adhesion strength. Therefore, rather than aiming to eliminate ice, a more practical approach is to minimize the ice adhesion strength, ideally close to zero [13]. While developing anti-icing materials (AIMs) with ultralow ice adhesion is achievable, several challenges must be addressed to optimize their performance. A realistic solution for all-weather outdoor anti-icing applications is to ensure that AIMs maintain an ice adhesion strength below 100 kPa, rather than striving for the absolute lowest possible value. Additionally, incorporating external stimuli such as photothermal and electrothermal heating can increase the ice removal efficiency, making it possible to shed ice quickly (within 5 min) while maintaining safety, reliability, and cost-effectiveness.

This review aims to summarize the design strategies in MXene-based anti-icing and deicing coatings, which are uniquely positioned to address the limitations of conventional passive materials. We will specifically focus on how the exceptional photothermal and electrothermal conversion characteristics of MXenes are being leveraged for both passive and active ice mitigation. Beginning with an overview of the fundamental photothermal and electrothermal conversion mechanisms of MXenes, this review will systematically examine various design strategies for MXene-based coatings and their performance in anti-icing and deicing applications. This comprehensive analysis will provide a critical roadmap for future research in the development of highly efficient, durable, and energy-effective anti-icing/deicing technologies.

2 Photothermal and electrothermal conversion mechanism of MXene

Photothermal materials, which can efficiently capture and convert solar energy into heat, have been the subject of extensive research in recent decades in various fields, e.g., water desalination, anti-icing/deicing, photocatalysis, photothermal therapy, and antibacterial applications [14]. For optimal performance, these materials must exhibit broadband absorption across the solar spectrum and a high solar-to-thermal energy conversion efficiency [15]. A wide range of nanostructured photothermal materials has been explored, including semiconductors [16], nanocarbon-based materials [14], MXenes [17], and polymers [18]. When exposed to sunlight, these materials absorb photons, initiating photoexcitation processes where charge carriers become mobilized under a light-induced electric field, ultimately leading to heat generation. The exact photothermal conversion mechanism varies depending on the electronic properties of the material and interaction with electromagnetic radiation, which are influenced by factors such as bandgap structure and electron dynamics. Broadly, photothermal conversion can be categorized into three fundamental mechanisms: (1) localized surface plasmon resonance (LSPR), (2) electron–hole pair excitation and recombination, and (3) delocalized electron interactions, including conjugation and hyperconjugation effects [19].

MXenes [20–22] are a class of 2D transition metal carbides, nitrides, and carbonitrides with a general formula of $M_{n+1}X_nT_x$, where T_x represents the surface functional groups, typically -O, -OH, -F, and/or -Cl. In addition to their high conductivity, their compact and highly aligned nature also endows $Ti_3C_2T_x$ films with high mechanical strength and toughness. The fundamentals of MXene synthesis are explained in Lim et al. [23]. $Ti_3C_2T_x$ exhibits an excellent electro and photothermal conversion performance and photo-to-heat conversion efficiency of nearly 100% and shows superior electromagnetic wave absorption ability [24]. On one aspect, concerning absorption width, MXenes exhibit typical semiconductor behavior characterized by a narrow bandgap due to their abundant surface functional groups. This characteristic results in broad absorption across the solar spectrum, providing a clear advantage over conventional wide-bandgap semiconductors. The latter, constrained to UV absorption, covers only a small portion of the solar spectrum, making MXenes more efficient in terms of photothermal conversion. On the other hand, the LSPR effect of MXenes highlights the responsivity across the UV–visible–NIR range, further enhancing photothermal conversion efficiency [19]. Among MXene family, $Ti_3C_2T_x$ has been commonly explored in various fields such as energy storage [25], sensing [26], electromagnetic interference (EMI) shielding [27], and biomedicine [28]; however, the investigation of its thermal management properties is in its infancy [17]. V_2CT_x and Nb_2CT_x are gaining attention among the MXene family. Nb_2CT_x was not exploited in the biomedical field until 2017 [29]. Maintaining a high light absorption ability in the NIR-I and NIR-II (950–1350 nm) windows, the photothermal conversion efficiency of Nb_2CT_x has been studied mainly in cancer therapy [30]. V_2CT_x MXene has a photothermal conversion efficiency of 48% [31]. However, neither of them has been investigated for deicing applications.

Joule heating, known as resistive heating or ohmic heating, is the process of converting electrical energy into thermal energy within a conductive material. As the current flows through the material, the electrons collide with the atoms, causing the atoms to vibrate more vigorously. This

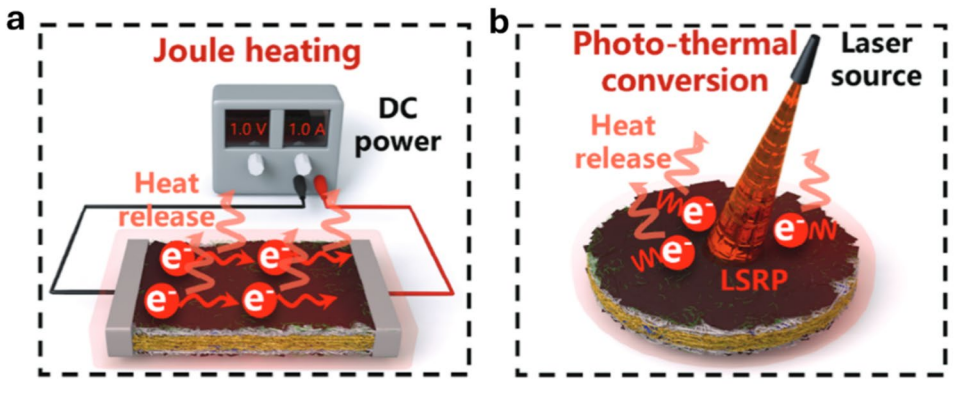

Scheme 1 **a** Schematic illustration of electrothermal and **b** photothermal conversion mechanism of MXene. Reproduced with permission from Wiley [33]

increased atomic vibration is perceived as heat. The electrothermal conversion mechanism of MXene is Joule heating [32]. A schematic illustration of the electro and photothermal conversion mechanism of MXene is shown in Scheme 1.

3 Photothermal deicing coatings

Slippery liquid-infused porous surfaces (SLIPS) utilize liquid lubricants such as silicone oil or ionic liquids (ILs) for anti-icing/deicing since these materials remain in a fluid state at low temperatures, low surface energy, and low ice adhesion strength. However, they have low mechanical and chemical durability. MXenes have been used to mitigate these limitations while increasing electro and photothermal efficiency.

The summary of photothermal deicing coatings is presented in Table 1. A 3D liquid-based porous coating was designed by Zhang et al. [34] (Scheme 2) using Mo_2CT_x MXene. At 100 mW cm^{-2} and the setting temperature of − 10 °C, the surface temperature of the coating reached 5.7 °C in 10 min, whereas that of the coating without MXene remained at − 8.2 °C, and the nonporous coating only reached 0.1 °C. Delayed ice formation of 3186 s at − 15 °C was observed, which was 33.2 times longer than that of a bare aluminum plate. The extremely low ice adhesion strength of 4.66 kPa was mainly due to the silicone oil layer remaining in a liquid state at low temperatures, along with the gradual diffusion of silicone oil from the oleogel sealer layer into the porous matrix during high-temperature curing. This diffusion lowered the interfacial modulus of the upper porous coating, playing a crucial role in reducing ice adhesion. Additionally, the high photothermal conversion efficiency of Mo_2CT_x, its uniform distribution in the matrix, and prolonged residence of the light in the porous structure highlight the suitability and durability of this design for practical anti-icing/deicing applications.

Inspired by Shell nacre's "brick-mud", Song et al. [35] designed a SLIPS by creating microstructure pits on an aluminum phosphate/$Ti_3C_2T_x$-coated Fe plate. This surface was then modified chemically with 3-mercaptopropyl trimethoxysilane to attach vinyl-terminated polydimethylsiloxane via Click reaction. This hydrophilic lubricant-grafted textured surface (LGTS) had a water contact angle (WCA) of 76.5° and a sliding angle (SA) of 4.28°. Compared with the bare Fe surface temperature of 40 °C, it reached a temperature of 55.6 °C in 600 s under 100 mW cm−2 Xenon light. Under 100 mW cm−2, an ice droplet slid off the surface when tilted 10° before completely melting, reducing the risk of secondary freezing. Delayed icing times of 27 and 335 s were observed for the bare Fe plate and coated surface, respectively, whereas the ice adhesion strength remained at approximately 20 kPa after 20 deicing cycles.

Zheng et al. [43] utilized an ambient-pressure-dried (APD) strategy to fabricate a lightweight, robust, and flexible aerogel. The polyurea aerogel was first dip-coated in $Ti_3C_2T_x$ dispersion, followed by spray-coating of GO, and finally crosslinking with PMDI. With an increasing power density of irradiated Xenon lamp from 50 to 250 mW cm^{-2}, a temperature increase from 39 to 116.2 °C in 500 s was observed, which also linearly increased with increasing MXene content.

Another aerogel composed of $Ti_3C_2T_x$ and graphene was designed by He et al. [42]. First, a graphene aerogel with a hierarchical architecture was prepared via unidirectional freezing followed by immersion in MXene dispersion and infiltration with epoxy resin. The conductivity of the aerogel, containing 23.85 wt% MXene, reached 74.08 S m^{-1}. Surface temperatures of 50 and 73 °C were measured at 100 and 200 mW cm^{-2}, respectively. A 3-mm-thick aerogel melted an ice droplet in 2 min at 100 mW cm^{-2}. When a water droplet was placed on the coating, which was already cooled to − 30 °C and then exposed to 100 mW cm^{-2} solar irradiation, no freezing occurred even after 5 min, whereas in the absence of MXene and graphene, it froze in 3 min. This study utilized the same conductive materials as Zheng et al. [43]; however, the design of the latter group with a

Table 1 The summary of the photothermal deicing coatings

Category	Ref	Publication year	Composition	MXene loading	Type of composite/thickness	WCA (°)/SA (°)	Heat source/photothermal properties	Mechanical properties
Photothermal coatings	[36]	2021	$Ti_3C_2T_x$/PDDA/poly(PFEMA)-co-poly(BMA)	NR	LBL film/10 μm	120/24	Xenon lamp/31 °C at 100 mW cm^{-2} in 10 min at an environmental temperature of −30 °C	NR
	[37]	2022	polyurethane-$Ti_3C_2T_x$@SnO_2	2.0 wt % $Ti_3C_2T_x$@SnO_2	Film/400 μm	85/NR	Xenon lamp/32.7 °C at 100 mW cm^{-2}	Break strength = 46.5 MPa elongation at break = 459%
	[38]	2023	$Ti_3C_2T_x$/PDA/[BHIM]NTf_2	0.04 wt% of $Ti_3C_2T_x$@PDA in IL	Nanofluid/NR	NR	Xenon lamp/73.9 °C at 100 mW cm^{-2}	NR
			$Ti_3C_2T_x$/PEI/[BHIM]NTf_2	0.04 wt% $Ti_3C_2T_x$@PEI in IL			Xenon lamp/71.5 °C at 100 mW cm^{-2}	
	[39]	2023	$Ti_3C_2T_x$-tanic acid-TDI/PU	4 wt%	Film/NR	105.4/NR	Sunlight/73.7 °C at 100 mW cm^{-2}	elongation at break = 412%
	[40]	2023	$Ti_3C_2T_x$/FCuS/PDA-IL	$Ti_3C_2T_x$/FCuS mass fraction 0.12%	Nanofluid/NR	NR	NR/80.2 °C under 100 mW cm^{-2}	NR
			$Ti_3C_2T_x$/HCuS/PDA/IL	$Ti_3C_2T_x$/HCuS mass fraction 0.12%	Nanofluid/NR	NR	NR/76.3 °C at 100 mW cm^{-2}	NR
	[41]	2024	$Ti_3C_2T_x$/carbon aerogel	29.4 wt%	Aerogel/NR	NR	Xenon lamp/94.5 °C in 50 s at 100 mW cm^{-2}	NR
	[42]	2024	PDA@GO/$Ti_3C_2T_x$/epoxy resin	23.85 wt%	Aerogel/3000 μm	NR	Solar irradiation/50 °C at 100 mW cm^{-2}	NR
	[43]	2024	cross-linked polyurea/MXene/GO	2 w%	Aerogel/NR	NR	Xenon lamp/116.2 °C in 500 s at 250 mW/cm^{-2}	NR
	[35]	2024	Fe@aluminum phosphate/$Ti_3C_2T_x$@3-mercaptopropyl trimethoxysilane@PDMS	NR	Lubrication film/NR	76.5/4.28	Xenon light/55.6 °C in 600 s at 100 mW cm^{-2}	NR
	[34]	2024	PDMS/expandable microspheres/oleophilic Mo_2CT_x	(Mo_2C:PDMS) (1:5)	Oleogel/NR	NR/11	Xenon lamp/5.7 °C in 600 s at 100 mW cm^{-2} at the setting temperature of −10 °C	Young's modulus = 3.46 Mpa

NR Not reported

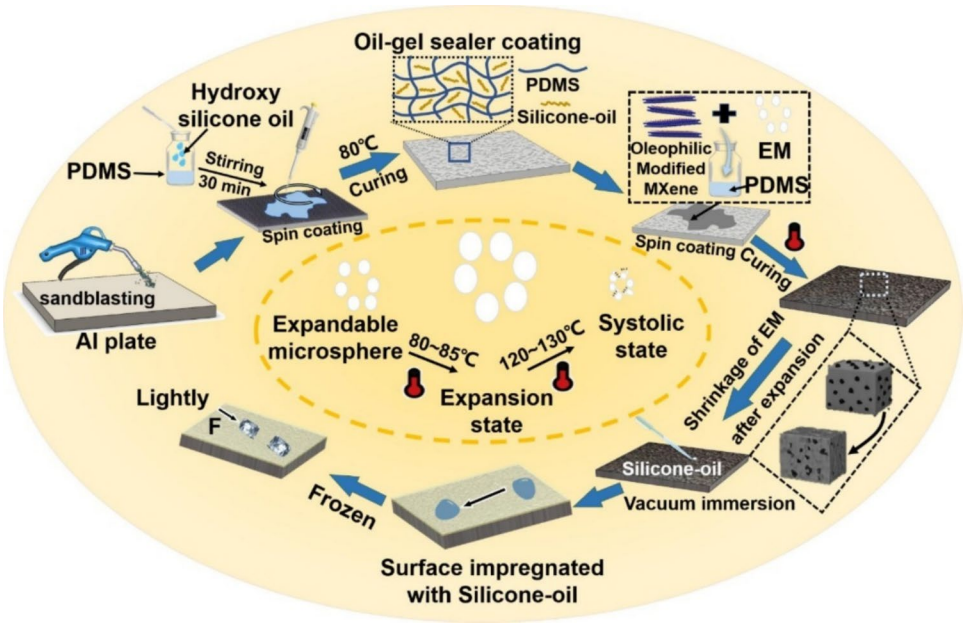

Scheme 2 Preparation of Mo_2CT_x/silicon oil SLIPS. Reproduced with permission from Elsevier [34]

much lower MXene content has led to higher photothermal conversion efficiency.

As a solution for pipeline blockage in real-life applications, Su et al. [38] designed $Ti_3C_2T_x$-IL-based nanofluids consisting of $Ti_3C_2T_x$@polydopamine (PDA) and $Ti_3C_2T_x$@polyetherimine (PEI) with imidazole IL [BHIM]NTf_2 due to their high thermal stability, efficiency, and low viscosity. When the content of $Ti_3C_2T_x$@PDA and $Ti_3C_2T_x$@PEI reached 0.04% in IL, under 100, 200, and 300 mW cm^{-2} irradiation with a Xenon lamp, the temperatures of $Ti_3C_2T_x$@PEI-IL reached 71.5, 93.6, and 104.7 °C. In contrast, those of $Ti_3C_2T_x$@PDA-IL showed slightly higher temperatures at 73.9, 106.0, and 119.7 °C, respectively, due to the additional photothermal effect of PDA. Leveraging the LSPR effect of MXene and the SPR effect and d–d transition of CuS, the same research group designed different nanofluids containing $Ti_3C_2T_x$/flower-shaped CuS ($Ti_3C_2T_x$/FCuS-IL) or hollow CuS ($Ti_3C_2T_x$/HCuS-IL) [40]. $Ti_3C_2T_x$/FCuS and $Ti_3C_2T_x$/HCuS were modified with PDA to improve the dispersion stability in the ILs. In five cycles of irradiation of 100 mW cm^{-2}, the nanofluids with $Ti_3C_2T_x$/CuS mass fraction of 0.12%, $Ti_3C_2T_x$/FCuS-IL, and $Ti_3C_2T_x$/HCuS-IL consistently reached temperatures of 80.2 °C and 76.3 °C, respectively, due to the greater photothermal conversion properties of FCuS.

A transparent ($T\% > 77\%$) self-healing solid omniphobic slippery (SOPS) coating by first layer-by-layer (LBL) assembly of negatively-charged $Ti_3C_2T_x$ and positively charged poly(diallyldimethylammonium) (PDDA) via dip-coating and finally blade-coating of melted poly(PFEMA)-*co*-poly(BMA) copolymer was fabricated at the meter scale (Fig. 1a) [36]. The 4-layer film with a thickness of 10 µm showed optimal photothermal properties increasing to 31 °C in 10 min under 100 mW cm^{-2} at an environmental temperature of − 30 °C (Fig. 1b). A 5-mm-thick ice block melted in 8 min under the same illumination intensity and slid off the surface. Notably, the self-cleaning ability of the $Ti_3C_2T_x$-SOPS coating could be restored through a cyclic etching–illumination process. Even after five cycles, the CA and SA of glycerol droplets remained virtually unchanged (Fig. 1c).

Liu et al. [41] fabricated $Ti_3C_2T_x$/carbon aerogel (CA) by obtaining CA from watermelon and dipping it in $Ti_3C_2T_x$ dispersion. With an optimized $Ti_3C_2T_x$ loading of 29.4 wt%, the surface temperature of the aerogel reached 94.5 °C in 50 s at 100 mW cm^{-2} (Fig. 2a). Evaporation rates of ~ 1.48, 3, and 4.5 kg m^{-2} h^{-1} were achieved under irradiations of 100, 200, and 300 mW cm^{-2}, respectively, for three cycles. Without sunlight, the ice partially melted at room temperature in 150 s (Fig. 2b), but under sunlight, it fully melted in 120 s and was quickly absorbed by the aerogel (Fig. 2c), showing the photothermal deicing properties. Moreover, $Ti_3C_2T_x$/CA absorbed low-viscosity oils and solvents without sunlight, but high-viscosity pump oil (99.45 mm^2 s^{-1} at 40 °C) remained on the surface of the aerogel until exposed to sunlight, which reduced its viscosity and allowed complete absorption within 150 s (Fig. 2d, e). The absorption capacities of some organic solvents and oils are shown in Fig. 2f.

Cui et al. [39] proceeded with in situ polymerization of tannic acid and toluene diisocyanate in the presence of $Ti_3C_2T_x$ (MXene-TT) before integrating it into polyurethane (PU) resin (MXene-TT/PU). The film containing 4 wt% MXene, had a WCA of 105.4° and thermal conductivity of

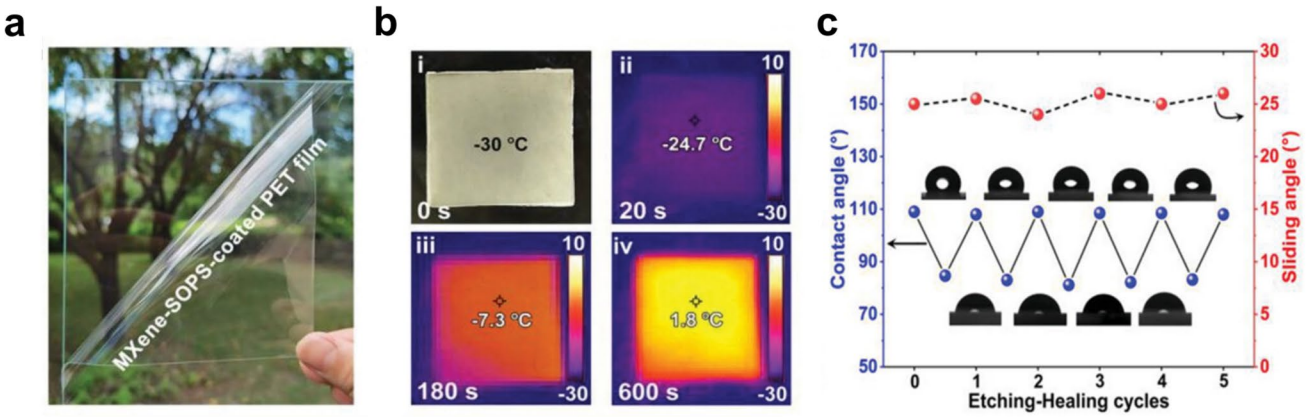

Fig. 1 **a** Photograph of the $Ti_3C_2T_x$-SOPS-coated PET affixable film applied on glass. **b** Photograph (i) and IR thermal images (ii–iv) of the $Ti_3C_2T_x$-SOPS-coated PET film after 100 mW $cm.^{-2}$ illumination for different durations at an atmospheric temperature of − 30 °C. **c** CAs (4 µL) and SAs (10 µL) of glycerol droplets on the $Ti_3C_2T_x$-SOPS-coated glass surface after undergoing different cycles of etching-healing treatments. Reproduced with permission from Wiley [36]

0.31 W m^{-1} k^{-1}. The maximum temperatures recorded were 57.1, 73.7, and 120.0 °C for MXene-TT/PU during 20 min exposure to simulated sunlight at intensities of 50, 100, and 200 mW cm^{-2}, respectively. In contrast, the temperature of pure PU under 100 mW cm^{-2} irradiation reached only 38.3 °C, highlighting the superior light absorption capability of the MXene-TT/PU nanocomposite. In deicing tests at − 20 °C under simulated sunlight, a 50-µL frozen water droplet on MXene-TT/PU attained an equilibrium temperature of 23.6 °C, compared to 1.0 °C for pure PU. Inspired by the antireflection phenomenon of moth eyes and cicada wings, Cai et al. [37] fabricated a multifunctional and biomimetic $Ti_3C_2T_x$@SnO_2 hierarchical nanostructure, thus enhancing the fire safety, solar deicing, and mechanical properties of thermal polyurethane (TPU) nanocomposites. The TPU-$Ti_3C_2T_x$@SnO_2 composite with 2.0 wt % $Ti_3C_2T_x$@SnO_2 content melted ice pellets in approximately 40 s at − 20 °C with a surface temperature of 32.7 °C under simulated solar irradiation of 100 mW cm^{-2}, which was far faster than the 600 s needed for pure TPU, positioning the TPU-$Ti_3C_2T_x$@SnO_2 composites for applications in extreme environments such as wind turbine blades and aircraft coatings.

4 Electrothermal deicing coatings

The summary of the electrothermal deicing coatings is presented in Table 2.

Deb et al. [32] used a controlled ultrafast Joule heating strategy for surface-limited crosslinking of PDMS over a $Ti_3C_2T_x$ aerogel (JPM) to avoid blocking all the micro/nanopores (Fig. 3a, b). The electrical conductivity of this aerogel was 67 S m^{-1}, which was higher than the oven-cured composite (OPM, 36 S m^{-1}) due to lower PDMS content. Compared with the OPM (WCA 113.4°), the flexible lightweight JPM had a markedly higher WCA of 143.6°. By applying 1.5, 2.5, 3.5, and 4 V, the temperature of the JPM increased to 58, 110, 166, and 213 °C, respectively, in 10 s and by switching off the input supply, the temperature rapidly dropped to 60% of its saturation value in 2 s due to the minimal coating of PMDS over the MXene aerogel. During 50 heating and cooling cycles, the thinly PDMS-coated MXene aerogel (100 µm) achieved a similar surface temperature and retained the response rate at an input voltage of 2.5 V, and presented a stable temperature for 3600 s. When 2.5 V was applied, a 100-µL supercooled water droplet melted in 92 s and slipped off the surface, indicating its high hydrophobicity and electrothermal performance (Fig. 3c).

Ag nanowires (NWs) offer numerous electrothermal pathways owing to their outstanding thermal and electrical conductivity. Integrating AgNWs into MXene nanosheets combines two highly conductive materials, addressing the limitations of AgNWs, which lack structural support and typically require a substrate. Furthermore, this combination helps lower the operating voltage of MXene films, which is typically higher than that of AgNWs [54].

A highly transparent (*T*%: 89.3%) film comprising PDMS-encapsulated $Ti_3C_2T_x$@AgNWs was prepared via spin-coating [51]. The temperature of this flexible electronic with a low resistance (15 Ω sq^{-1}) operated steadily during 20 cycles, increasing from 32 to 57 °C in 15 s by applying 2 V and melting an ice cube completely in 10 min under 5 V. Xia et al. [54] utilized vacuum-assisted filtration (VAF) to develop a flexible asymmetric "Mille-Feuille"-like MXene – MXene@AgNWs-MXene-AgNWs film (Scheme 3). The 9.02-µm-thick film exhibited remarkable electrical conductivity, with the conductivity on the $Ti_3C_2T_x$

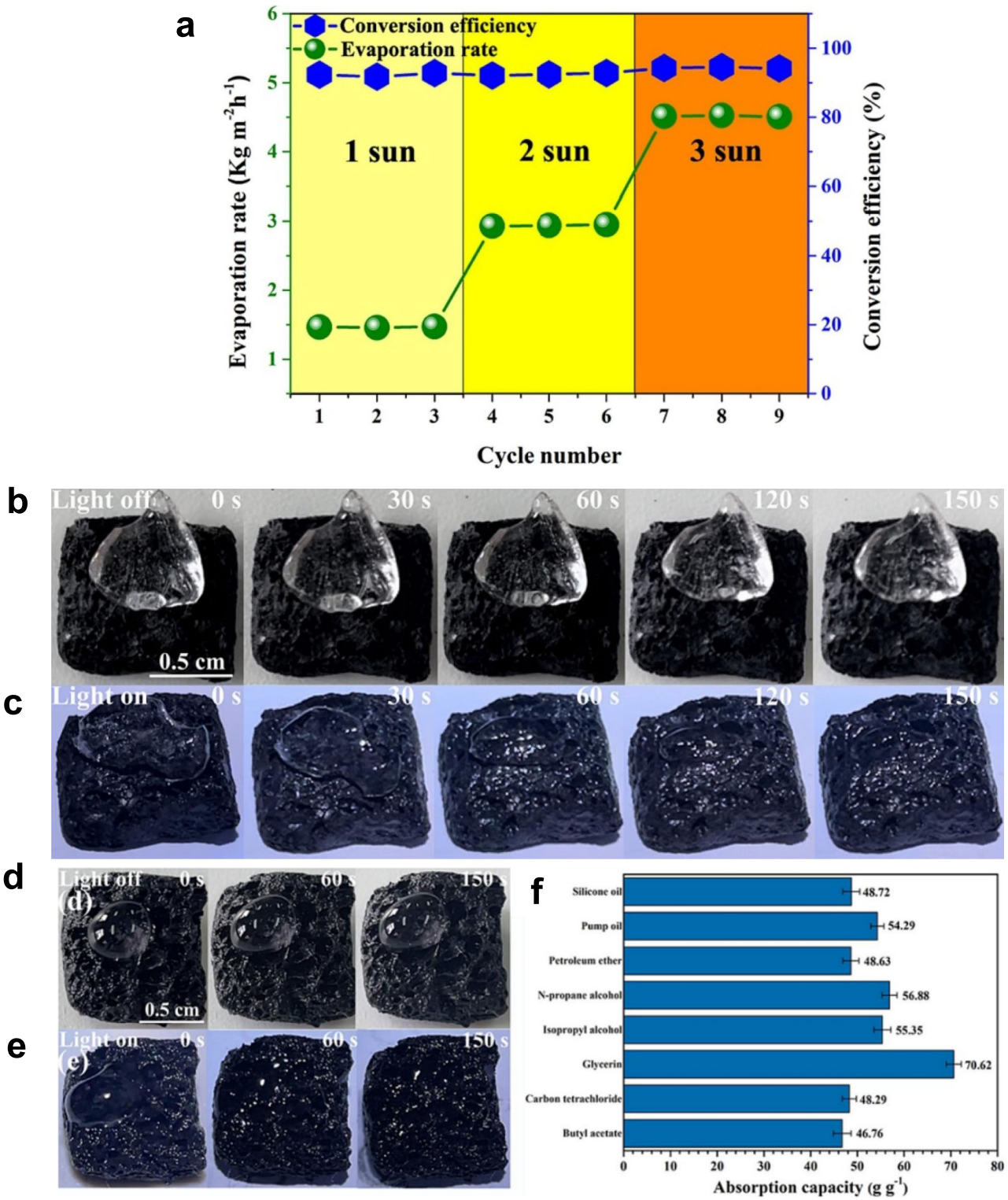

Fig. 2 **a** Performance of $Ti_3C_2T_x$/CA under sunlight with different sunlight intensities after three cycles. Deicing processes on $Ti_3C_2T_x$/CAs **a** with and **c** without sunlight irradiation. Absorption of a viscous oil by $Ti_3C_2T_x$/CA **d** with and **e** without sunlight irradiation. **f** Absorption capacity of $Ti_3C_2T_x$/CA. Reproduced with permission from Elsevier [41]

Table 2 The summary of the electrothermal deicing coatings

Category	Ref	Publication year	Composition	MXene loading	Type of composite/thickness	WCA (°)/SA (°)	Electrothermal properties	Electrical conductivity/resistance	Ice melting time	Mechanical properties
Electrothermal coatings	[44]	2021	Epoxy resin/$Ti_3C_2T_x$	10 w%	Aerogel	NR	43, 127, and 166 °C at 1, 2, 3 V in 160 s	210 S cm^{-1}	NR	NR
	[45]	2021	$Ti_3C_2T_x$/TPU	28.6 wt%	Multilayered film/52 μm	NR	39.6 °C and 113 °C at 2 and 5 V in 10 s	1600 S m^{-1}	Ice melted in 540 s at 5 V	Tensile fracture strain = 808% tensile strength = 38.6 MPa
	[46]	2022	$Ti_3C_2T_x$/PI	49.1 wt%	Film/256 μm	NR	38, 42.5, 65, 75, 93, and 105 °C at 1, 1.2, 1.5, 1.8, 2.3, and 2.5 V in 10 s	3787.9 S m^{-1}	Ice melted in 120 s at 2.3 V	Young's modulus = ~600 MPa
	[47]	2022	$Ti_3C_2T_x$@CF (5 layers)	NR	Film	NR	53.7 °C at 0.088 W cm^{-1} in 180 s	245.9 Ω	Ice melted in ~5 min at 0.088 W cm^{-1}	NR
			PEDOT/CNT@CF (8 layers)				58.9 °C 0.088 W cm^{-1} in 180 s	3093.9 Ω		
	[48]	2023	CoC@CNF/$Ti_3C_2T_x$	NR	LBL film/50 μm	NR	28, 34, 41, 80, and 138 °C, at 5, 6, 7, 8, and 10 V in 100 s	94 S m^{-1}	Ice melted in 240 s at 10 V	Young's modulus = 40 MPa, elongation at break = 8%
	[49]	2023	$Ti_3C_2T_x$-WPU-Co/C	21.8 w%	Aerogel/40 μm	NR	41.1, 51.2, 113.1 °C at 2, 3, 4 V	NR	Ice melted in 190 s at 4 V	NR
	[50]	2023	$Ti_3C_2T_x$-NiCF/epoxy	NR	Film/1 mm	47.2/NR	36, 45, 64, 76, 101 °C, at 0.5 to 0.7, 1, 1.2, 1.5 V in 150 s	4570 S m^{-1}	NR	NR
	[51]	2024	$Ti_3C_2T_x - Ti_3C_2T_x$@AgNWs-$Ti_3C_2T_x$-AgNWs	NR	LBL film/9.02 μm	NR	56.4 °C@0.3 V, 77 °C@0.4 V, 100.6 °C@0.5 V, 127.7 °C@0.6 V, 154.2 °C@0.7 V, 189.8 °C@0.8 V, 206.2 °C@0.9 V, 227.7 °C@1.0 V in ~35 s	2217 S cm^{-1}	NR	NR
	[32]	2024	$Ti_3C_2T_x$/PDMS	NR	Aerogel/100 μm	143.6/NR	58, 110, 166, and 213 °C at 1.5, 2.5, 3.5, and 4 V in 10 s	6700 S m^{-1}	Ice melted in 92 s at 2.5 V	NR

Table 2 (continued)

Category	Ref	Publication year	Composition	MXene loading	Type of composite/thickness	WCA (°)/SA (°)	Electrothermal properties	Electrical conductivity/resistance	Ice melting time	Mechanical properties
	[52]	2024	$Ti_3C_2T_x$/densified wood	NR	Film/NR	NR	55, 103, and 162 at 2 V, 4 V, and 6 V in 40 s	830 Sm^{-1}	Ice melted in 120 s at − 15 °C at 6 V	Tensile strength = 424.7 MPa Young's modulus = 14.6 GPa
	[51]	2024	PDMS@$Ti_3C_2T_x$/AgNWs	NR	Film/NR	NR	From 32 to 57 °C in 15 s by applying 2 V	15.1 Ω sq^{-1}	Ice melted in 10 min at 5 V	NR
	[53]	2024	$Ti_3C_2T_x$/Fe_3O_4@CNTs/TOCNF	$Ti_3C_2T_x$/Fe_3O_4@CNTs 95 wt%	Nanopaper/18 µm	NR	40 and 78 °C at 4.5 V in a few seconds	11,111 S m^{-1}	Ice melted in 420 s at 4 V	NR

NR Not reported

surface reaching 2217 S cm^{-1} and that on the AgNWs surface reaching 3659 S cm^{-1}. Significantly high equilibrium temperatures in a range of low applied voltages were achieved at 56.4 °C@0.3 V, 77 °C@0.4 V, 100.6 °C@0.5 V, 127.7 °C@0.6 V, 154.2 °C@0.7 V, 189.8 °C@0.8 V, 206.2 °C@0.9 V, and 227.7 °C@1.0 V, respectively, in ~35 s indicating a sensitive response. Compared to the blending method, this LBL design has demonstrated superior performance.

In $Ti_3C_2T_x$/epoxy thermal heaters, MXene performs as a nanoheater, whereas the epoxy resin spreads heat. A 3D MXene/epoxy aerogel with excellent Joule heating capability was fabricated via VAF of epoxy into unidirectionally freeze-dried $Ti_3C_2T_x$ aerogel [44]. With 10 wt% $Ti_3C_2T_x$ loading, the aerogel exhibited the electrical conductivity of 2.1 S cm^{-1} and a temperature increase to 43, 127, and 166 °C by applying voltages of 1, 2, and 3 V, respectively, outperforming MXene thin film [55]. Electrophoretic deposition (EPD) was used to uniformly deposit negatively charged $Ti_3C_2T_x$ on Ni-modified carbon fibers with the main purpose of developing a tri-core–shell epoxy-based carbon fiber reinforced polymer (CFRP) composite [50]. The 1-mm-thick multifunctional composite with an electrical conductivity of 4570 S m^{-1} exhibited a temperature increase to 36, 45, 64, 76, and 101 °C in 150 s as the applied voltage increased from 0.5 to 0.6, 1, 1.2, and 1.5 V, respectively.

A gradient layered $Ti_3C_2T_x$/Fe_3O_4@CNTs/TEMPO-oxidized CNF (TOCNF) nanopaper (18 µm) was prepared via VAF which exhibited a high electrical conductivity of 11,111 S m^{-1} (Scheme 4) [53]. The film containing 95 wt% $Ti_3C_2T_x$/Fe_3O_4@CNTs exhibited an electrothermal response of 40 °C at 3.0 V and 78 °C at 4.5 V and melted a 1.5 cm^3 ice cube in 420 s at an applied voltage of 4 V, whereas it took 1600 s to melt naturally.

Spray coating was used to separately deposit $Ti_3C_2T_x$ and PEDOT/CNT on carbon fibers (CFs) [47]. A similar deicing time of 5 min at a power density of 0.088 W cm^{-1} was observed for $Ti_3C_2T_x$@CF (five layers) and PEDOT/CNT@CF (eight layers) coatings, whereas different resistances of 245.9 and 3093.9 Ω were observed. Under the same power density and duration, the average temperature increase was 84% greater for the $Ti_3C_2T_x$ coating and 117% greater for PEDOT-CNT coatings. As a result, both nanocoatings enabled deicing up to three times faster than fiber-based coatings.

A sandwich structure was designed by placing $Ti_3C_2T_x$/waterborne PU (WPU) aerogel between two Co/C-WPU and subsequently hot-pressing [49]. With optimized MXene content of 21.8 wt% and a thickness of 40 µm, the film presented a thermal conductivity of 3.29 W m^{-1} K^{-1} which was 1600% larger than that of pure WPU. When exposed to 2, 3, and 4 V external voltages, the surface temperature of the film reached 41.1, 51.2, and 113.1 °C, respectively, and

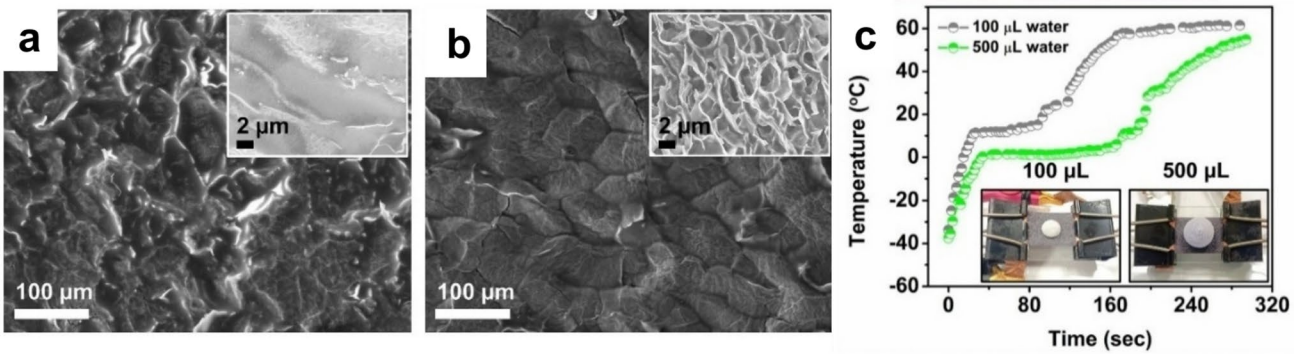

Fig. 3 FESEM images of the top surfaces of **a** OPM and, **b** JPM aerogels (inset shows their cross-sectional view). **c** Ice-to-water temperature conversion curve of the deicing process of a 100-μL and 500-μL supercooled water droplet at 2.5 V. Reproduced with permission from Elsevier [32]

an ice cube was melted in 190 s at 4 V. A flexible multilayered MXene/TPU film (MXene6-TPU5, the number refer to the number of spray coating times), composed of 28.6 wt% MXene and a thickness of 52 μm, was prepared via spray-coating, and demonstrated a high electrical conductivity of 1600 S m^{-1} [45]. Additionally, the film achieved a high in-plane thermal conductivity of 6.31 W m^{-1} K^{-1} while maintaining a low cross-plane thermal conductivity of 0.42 W m^{-1} K^{-1}. At 2 and 5 V, the temperature of the film reached 39.6 °C and 113 °C, respectively, within 10 s. An ice cube of 3 cm^3 melted completely in 540 s at 5 V. Polyimide (PI) is well-known for its flexibility, mechanical, and chemical durability. We recently published a review on the application of MXene/PI composites [20]. A $Ti_3C_2T_x$/PI film with a "rebar-brick-cement" lamellar structure was fabricated via VAF [46]. This film, with a thickness of 256 μm and MXene content of 49.1 wt%, had a high electrical conductivity of 3787.9 S m^{-1}, and the Young's modulus of ~ 600 MPa. The electrothermal characteristics of this film were evaluated as a fast response (10 s), during which the temperatures of 38, 42.5, 65, 75, 93, and 105 °C under low voltages of 1, 1.2, 1.5, 1.8, 2.3, and 2.5 V, respectively, were obtained. When 2.3 V was applied, an ice cube that was placed on the film melted within 120 s.

Ran et al. [48] created a series of CoC@CNF/$Ti_3C_2T_x$ composite films with a carefully designed LBL assembly of CoC/CNF and MXene via VAF. In this study, Co/C nanoparticles, produced by pyrolyzing ZIF-67, were used as the magnetic component. The thickness of the film was fixed at 50 μm regardless of the number of layers. The five-layer film showed an electrical conductivity of 94 S m^{-1} which was higher than that of the film prepared by blending CoC, CNF, and $Ti_3C_2T_x$ (32 S m^{-1}). The temperature of the five-layer CoC@CNF/$Ti_3C_2T_x$ film reached 28, 34, 41, 80, and 138 °C, at the voltage of 5, 6, 7, 8, and 10 V, respectively, within 100 s. When 10 V was applied, the ice cube melted completely within 240 s.

Zhang et al. [52] developed lightweight, ultrastrong, and multifunctional $Ti_3C_2T_x$/densified wood (MXene/DW) composite films. After DW was treated with a Cu^{2+} solution to obtain an ion-coordinated wood veneer, it was immersed in a $Ti_3C_2T_x$ aqueous dispersion under vacuum. The film showed the electrical conductivity of 830 S m^{-1} and demonstrated rapid electrothermal conversion, achieving steady-state temperatures of 55, 103, and 162 °C in 40 s at 2, 4, and 6 V, respectively, and returned to room temperature within 30 s after the voltage cutoff. At an environmental temperature of − 15 °C and under 6 V, the film melted the ice in 120 s, demonstrating its efficient deicing capability. The long-term stability was maintained under 4 V for 3500 s without significant performance degradation. The resistance of structural stability under harsh environmental conditions was tested in 3 M H_2SO_4 (Fig. 4a), 3 M NaOH (Fig. 4b), and 3 M NaCl (Fig. 4c) solutions for 7 days, at high (120 °C) (Fig. 4d) and low temperatures (Fig. 4e) (− 15 °C). The film showed no shedding of MXene, indicating its strong attachment to the wood. After the abovementioned exposures, the electrode provided a constant and stable current for LED lighting (Fig. 4f).

5 Combination of photothermal and electrothermal strategies

This section discusses the composition and efficiency of the composites with combined electro and photothermal properties (Table 3). PDMS has been used in several studies to introduce the following characteristics. It is hydrophobic, highly flexible due to its low Young's modulus, transparent, thus enhancing light absorption during photothermal conversion, and durable under harsh conditions, which can encapsulate active materials to protect them from oxidation. These attributes make PDMS one of the most promising candidates for applications in flexible functional materials [56].

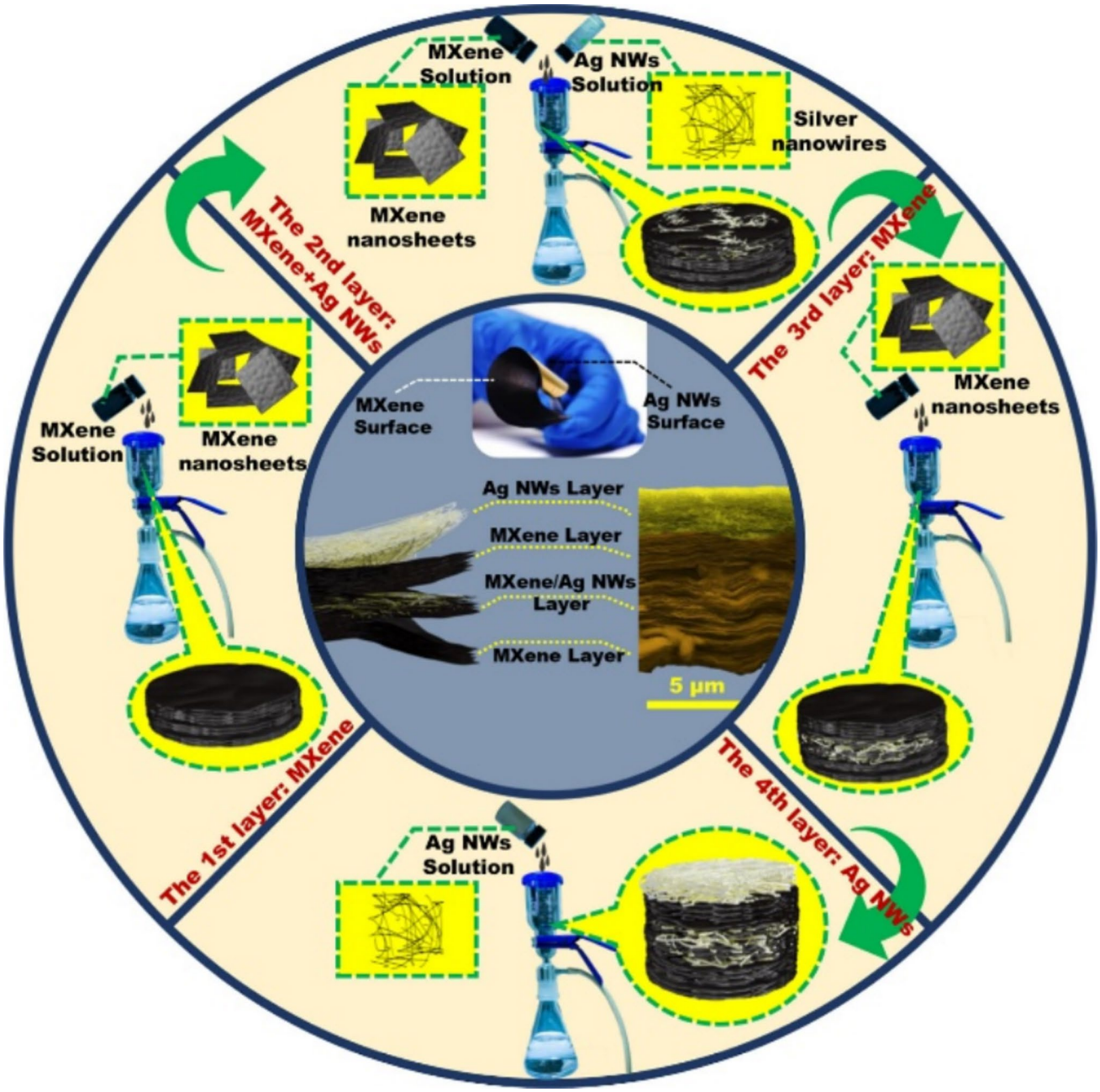

Scheme 3 Schematic of the fabrication procedure of the MXene–MXene@AgNWs-MXene-AgNWs hybrid films. Reproduced with permission from ACS [54]

A PDMS-encapsulated, two-layer film composed of a CNT upper layer and a $Ti_3C_2T_x$ bottom layer was fabricated via VAF for efficient photothermal and electrothermal conversion [57]. This dual-driven heating mechanism enables effective deicing, melting a 1000-mg ice layer in 223 s under a 2.5 V input and in 269 s under 200 mW cm^{-2} radiation. Figure 5a illustrates the photothermal test method. The light source can be a Xenon lamp, NIR laser, sunlight, or simulated solar light. An IR thermal camera is used to record the temperature. With a low resistance of 11.7 Ω, the 100-μm film reached a surface temperature of 89 °C at 2.5 V. Irradiation intensities of 100, 200, and 300 mW cm^{-2} resulted in surface temperatures of 61.3 °C, 84.5 °C, and 121.7 °C, respectively, stabilizing within 200 s. Additionally, the CNT layer enhanced the photothermal properties of the film, as shown in Fig. 5b. While ice formed on the film within 827 s, water droplets took longer (1425 s) to freeze due to surface microstructures and trapped air, which reduced heat transfer.

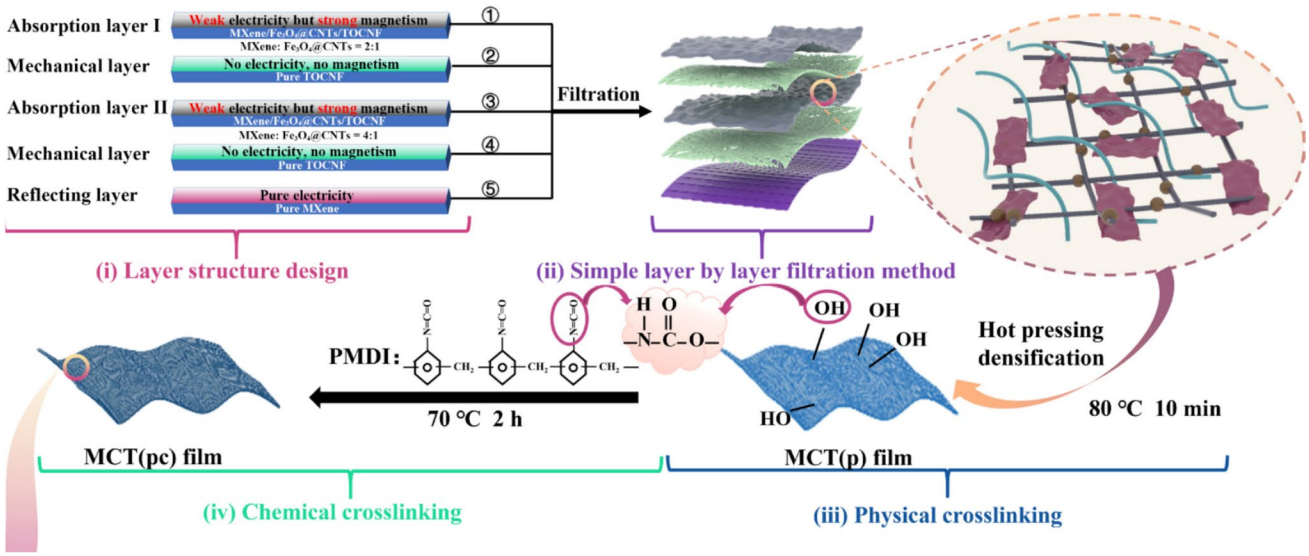

Scheme 4 Step-by-step demonstration of the fabrication of gradient layered $Ti_3C_2T_x$/Fe_3O_4@CNTs/TEMPO-oxidized CNF (TOCNF) nanopaper. Reproduced with permission from Springer Nature [53]

Li et al. [58] fabricated a superaligned CNT (SA-CNT)/crosslinked $Ti_3C_2T_x$ via immersion of high-strength, ultrathin, porous SA-CNT films into MXene dispersion and further crosslinking with PDMI. The film with $Ti_3C_2T_x$ content of 65 wt% and thickness of 9 µm had a significantly high Young's modulus of 13.8 GPa, and optimized electro and photothermal properties were achieved. The surface temperature of the film reached 128 °C at 200 mW cm^{-2} and 31, 54, 81, and 130 °C at 0.6, 1.2, 1.8, and 2.4 V, respectively. A block of ice slid off the film after 60 s of applying 2.4 V.

A PDMS/Ag@$Ti_3C_2T_x$ PET textile was fabricated by dip-coating PET textile in a Ag/MXene dispersion, followed by soaking in PDMS solution and curing [62]. Ag NPs facilitate charge transfer between the MXene sheets and prevent the sheets from re-stacking. When 3 V was applied, the temperature of the film rose to 105.4 °C in 10 s, and it took 742 s for an ice cube to melt completely. Under 100 mW cm^{-2} irradiation using a Xenon lamp for 10 min, the temperature of 73.1 °C was recorded. Another PDMS-encapsulated film was prepared by spray-coating a TEMPO-oxidized CNF/$Ti_3C_2T_x$ dispersion onto bacterial cellulose (Si-TM/BC) to obtain a 2.29-µm film with a low resistance of 5 Ω sq^{-1} (Fig. 6a) [59] which showed a temperature increase to 50, 90, and 130 °C at 2, 3, and 4 V, respectively, in less than 100 s, and an ice block of 5-mm-thick melted completely in 4 min at 3 V (Fig. 6b). After 30 cycles, the electrothermal performance of the textile could still exceed 100 °C at a constant voltage of 3 V. Under irradiation of 100 mW cm^{-2}, the surface temperature of the film increased to 90 °C in 300 s. After applying a constant voltage of 3 V for 600 s, the equilibrium temperature of the film reached 96 °C. To test the stability of the Si-TM/BC film, it was soaked in aqueous solutions with pH = 1 and pH = 7 for 24 h. The water evaporation efficiency of approximately 0.58 g h^{-1}, flame retardancy, and stability in acidic and alkaline media indicate promising application in the thermal management of textiles under extreme conditions. A comparison of the results of this study with those of Zhang and Guo [62] revealed the effect of Ag NPs on improved thermal properties.

A combination of $Ti_3C_2T_x$ and GO as active materials was spray-coated on a cellulose film [60]. With MXene content of 52 wt% and thickness of 23 µm, the electrical conductivity of the film reached 15,320 S m^{-1}. The temperatures increased rapidly from 22 to 35, 43, 74, 92, and 124 °C at light power densities of 25, 50, 100, 150, and 200 mW cm^{-2}, respectively. When voltages of 0.5, 1, 1.5, 2, and 2.5 V were applied, the surface temperature increased to 32, 48, 62, 88, and 113 °C, respectively. When the film was tilted 20°, under a voltage of 2.5 V, an ice block was melted and slid away in 60 s.

A multifunctional composite film of aramid nanofiber/cellulose nanofibril-modified $Ti_3C_2T_x$/AgNW-modified cellulose nanocrystals with high mechanical strength and conductivity was developed by Hu et al. [63]. This 22.88-µm-thick nanopaper exhibited an electrical conductivity of 1139.48 S cm^{-1} reaching a remarkable temperature of 215.35 °C at a power density of 1.36 W cm^{-2} (Fig. 7a, b) and 242.78 °C under 3 V in 5 s (Fig. 7c, d). Figure 7e shows that by applying an external voltage, an ice block melted completely in 250 s. $Ta_4C_3T_x$ MXene was one of the MXenes, other than $Ti_3C_2T_x$, investigated for anti-icing/deicing [61]. The lightweight porous $Ta_4C_3T_x$/graphene aerogel reached a surface temperature of 90.2 °C

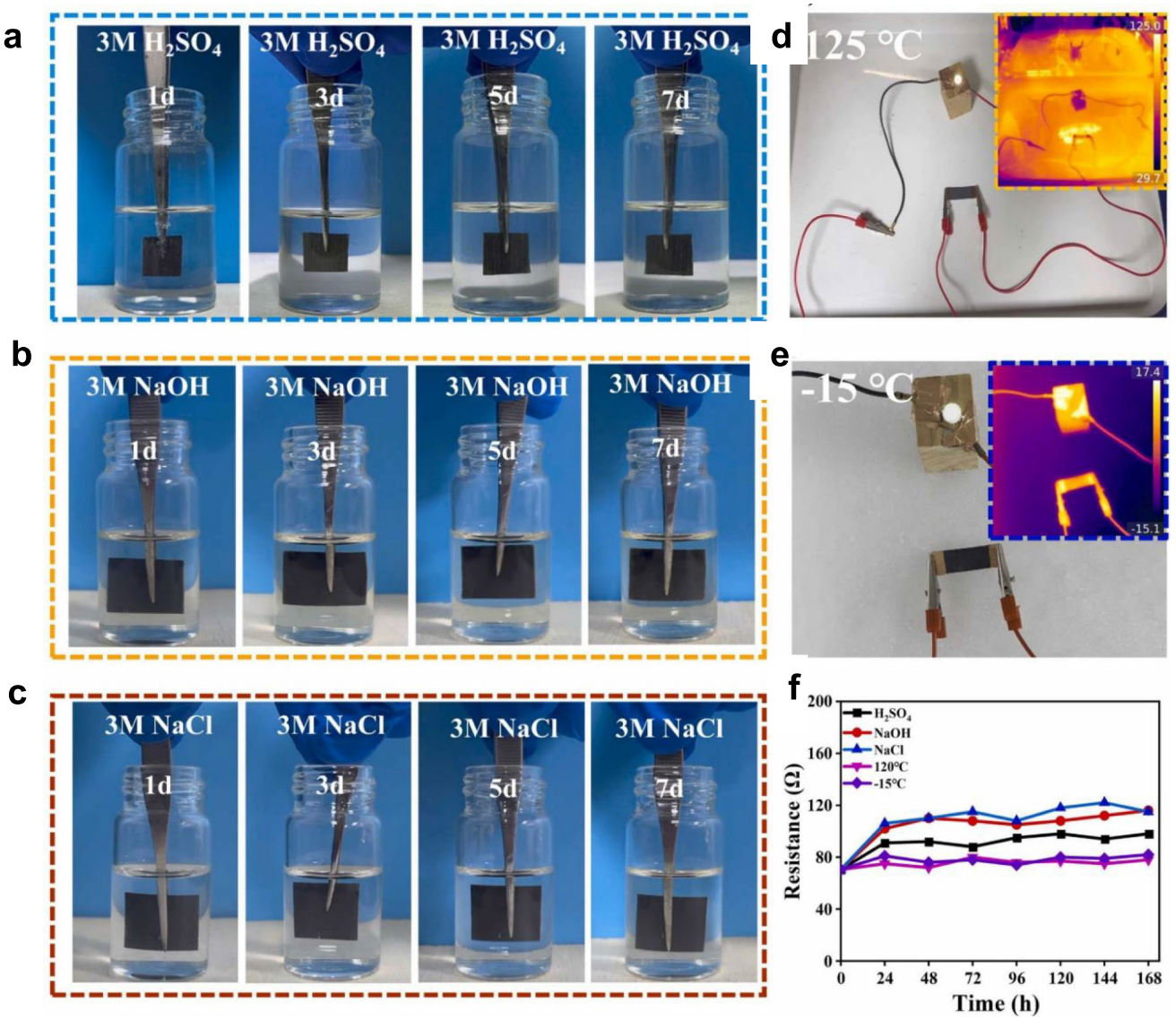

Fig. 4 Digital photos of the MXene/DW film in **a** 3 M H_2SO_4, **b** 3 M NaOH, **c** 3 M NaCl, **d** 125 °C high temperature, **e** − 15 °C low temperature, **f** resistance variations of the MXene/DW film in different harsh environments over a defined period. Reproduced with permission from Elsevier [52]

within 1 min under 100 mW cm^{-2} and to 30.2, 50.4, 72.5, and 99.4 °C within a very short time of 0.5 s by applying voltages of 1, 2, 3, and 4 V, respectively. Upon exposure to sunlight, an ice block placed on top of the aerogel melted completely in 120 s, while naturally, it took more than 180 s. The authors reported an electrical conductivity of 0.45 S m^{-1} for $Ta_4C_3T_x$/graphene aerogel sample compared with the $Ti_3C_2T_x$/graphene aerogel sample (0.14 S m^{-1}). The aerogel absorbed various oils 40–70 times its weight due to hydrogen bonding, π–π interactions, and electrostatic attraction between $Ta_4C_3T_x$ and graphene with contaminant molecules.

6 Combination of photo/electrothermal and superhydrophobic strategies

This strategy combines passive anti-icing via surface superhydrophobicity and active deicing via electro/photothermal properties (Table 4).

Owing to the combined effect of low-surface-energy chemistry and micro/nanoscale hierarchical structures, SHSs effectively repel incoming water droplets and reduce interfacial heat transfer under various conditions. Low ice adhesion strength is mainly observed on such surfaces. Secondary freezing is also inhibited without continuous electrothermal heating, depending on water repellency. Heating SHSs can

Table 3 The summary of the combination of photothermal and electrothermal coatings

Category	Ref	Publication year	Composition	MXene loading	Type of composite/thickness	WCA (°)/SA (°)	Photothermal properties	Electrothermal properties	Electrical conductivity/resistance	Ice melting time	Mechanical properties
Combination of photothermal and electrothermal strategies	[59]	2021	PDMS@TCNF/$Ti_3C_2T_x$-coated BC	NR	Film/2.29 μm	121/NR	Sunlight/90 °C at 100 mW cm^{-2} in 300 s	50, 90, and 130 °C at 2, 3, and 4 V in 100 s	5 Ω sq^{-1}	Ice melted in 4 min at 3 V	Mechanical strength = 250 MPa
	[57]	2022	$Ti_3C_2T_x$/CNT/PDMS	NR	Layered film/110 μm	128°/36.6°	NIR, 61.3 °C at 100 mW cm^{-2} in 200 s	89 °C at 2.5 V	11.7 Ω sq^{-1}	Ice melted in 269 s at 200 mW cm^{-2} and in 223 s at 2.5 V	NR
	[58]	2022	Superaligned CNT/crosslinked $Ti_3C_2T_x$	65 wt%	Film/9 μm	105/NR	Xenon lamp/128 °C at 200 mW cm^{-2}	31, 54, 81,130 °C at 0.6, 1.2, 1.8, 2.4 V	NR	Ice melted in 60 s at 2.4 V	Young's modulus = 13.8 GPa
	[60]	2023	Cross-linked GO/$Ti_3C_2T_x$/cellulose	52 wt%	Film/23 μm	105/NR	Xenon lamp/74 °C at 100 mW cm^{-2}	32, 48, 62, 88, 113 °C at 0.5, 1.0, 1.5, 2.0, 2.5 V	15,320 S m^{-1}	Ice melted in 60 s at 2.5 V on a 20° slope	Mechanical strength = 324 MPa
	[61]	2024	$Ta_4C_3T_X$/graphene	$Ta_4C_3T_X$/graphene: 3.84	Aerogel/NR	NR	Xenon lamp/90.2 °C at 100 mW cm^{-2} in 60 s	30.2, 50.4, 72.5, 99.4 °C at 1, 2, 3, 4 V in 0.5 s	0.45 S m^{-1}	Ice melted in 120 s in sunlight	NR
	[62]	2024	PDMS/Ag@$Ti_3C_2T_x$/PET	NR	Textile/NR	148/NR	Xenon lamp/73.1 °C at 100 mW cm^{-2} in 600 s	105.4 °C at 3 V in 10 s	NR	Ice melted in 742 s at 3 V	NR
	[33]	2025	Aramid nanofibers/cellulose nanofibrils modified $Ti_3C_2T_x$/cellulose nanocrystals and AgNWs	NR	Nanopaper/22.88 μm	NR	NR/215.35 °C at 1.36 W cm^{-2} in 5 s	242.78 °C at 3 V in 5 s	113,948 S m^{-1}	Ice melted in 250 s at 3 V	Tensile strength = 701.82 MPa

NR Not reported

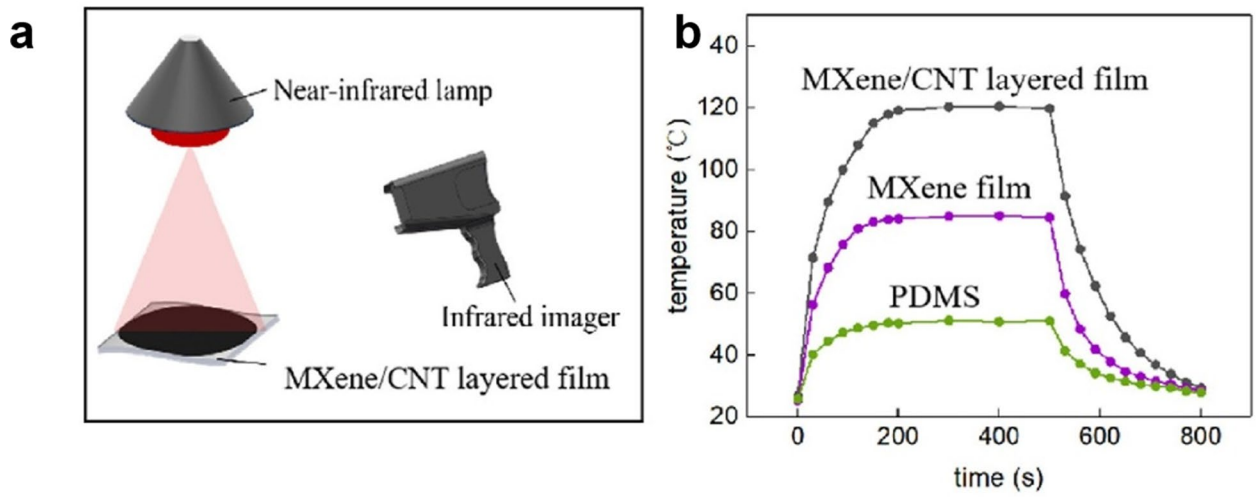

Fig. 5 **a** Schematic diagram of the photothermal property test. **b** Curves of the surface temperature with time at different irradiation intensities. Reproduced with permission from Elsevier [57]

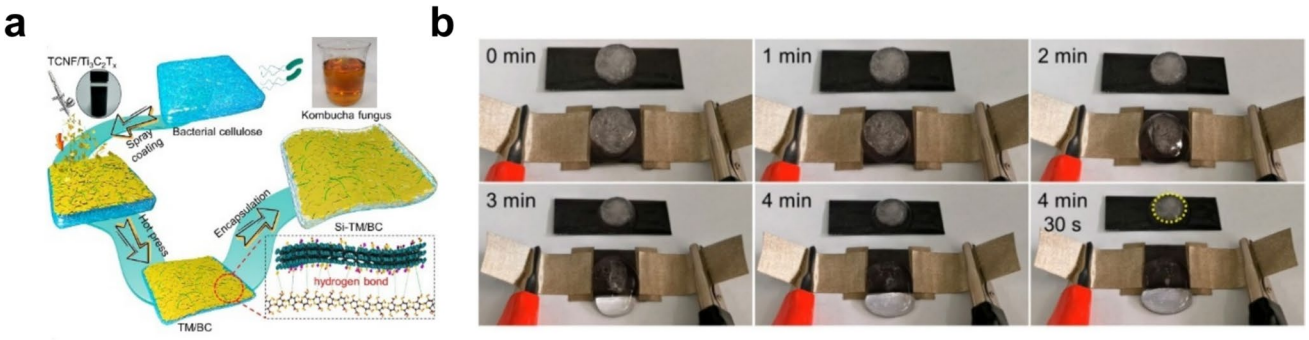

Fig. 6 **a** Fabrication strategy of the Si-TM/BC film. **b** Melting ice by applying 3 V. Reproduced with permission from ACS [59]

extend the longevity of the air layer by reducing vapor condensation caused by low temperatures during the freezing process. Additionally, it accelerates the regeneration of the air layer by facilitating droplet coalescence, which promotes their removal during the deicing process [70].

Surface modification can be applied to enhance the antioxidant properties of MXenes while preserving their inherent photothermal performance. This process also strengthens the bonding force and interfacial compatibility between MXene and polymers, ultimately improving the quality and durability of MXene-based polymer coatings. The MXene–based superhydrophobic surface was obtained via spray-coating fluorinated $Ti_3C_2T_x$, hydrophobic SiO_2 NPs, epoxy, and PDMS (MX–SHC), followed by curing on various surfaces (Fig. 8a) [70]. The optimized sample containing 5 wt% fluorinated MXene showed a WCA of 158° and SA of 4°, which remained constant on various substrates (Fig. 8b) and altered MXene content (Fig. 8c). The self-cleaning abilities of the coated glass and the uncoated glass were compared in Fig. 8d, e, respectively. Under irradiation at 100 mW cm^{-2}, the surface temperature increased to ~ 75.9 °C and ~ 20.1 °C rapidly at background temperatures of 25 °C and – 30 °C, respectively, completely melting a frozen droplet in 240 s at – 30 °C. A very low ice adhesion strength of 15 kPa was reported, which was significantly lower than that of the bare steel (– 144 kPa). The freezing of 150-µL droplet was delayed to 450 s, 256 s, and 122 s at – 10 °C, – 20 °C and – 30 °C, respectively, compared with that of pristine glass (59 s at – 20 °C), indicating its potential use in harsh cold environments.

In a different approach, a plasmonic $Ti_3C_2T_x$@Au–WPU coating was spray–coated with fluoroalkyl silanes (f–SiO_2) to achieve superhydrophobicity of 153° and an SA of 4.5° [64]. Under the irradiation of 500 mW cm^{-2}, the temperature reached 120 °C, and an ice cube of 3-mm-thick completely melted in 60 s, whereas in the case of the coating without f–SiO_2 more than half of the ice was still present. Compared with that of the coating without f–SiO_2 (212 s), an

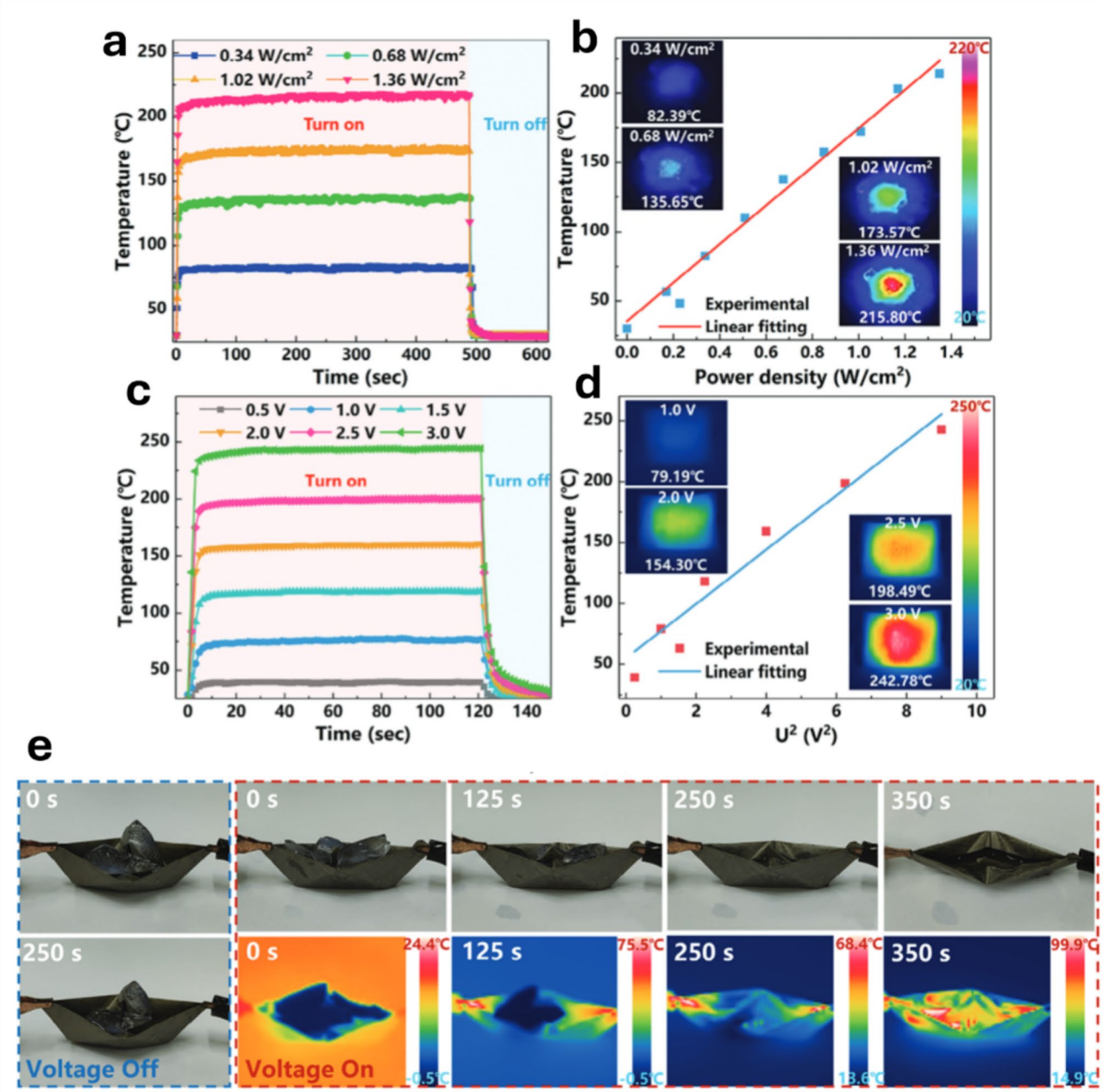

Fig. 7 **a** Photothermal heating performance of the nanopaper at different power densities. **b** Experimental data showing the linear correlation between the equilibrium temperature of the nanopaper and the power density. **c** Joule heating performance of the nanopaper. **d** Relationship between the equilibrium temperature of the nanopaper and the square of the applied voltage. **e** Nanopaper folded into a boat used for deicing ice blocks. Reproduced with permission from Wiley [63]

ultralong anti-icing time of 1053 s at − 20 °C was observed. A layered film of $Ti_3C_2T_x$/AgNWs (bottom) and N–boroxine–PDMS/SiO_2 NPs (top) was fabricated on PET via spray-coating (Fig. 9a) [71]. SEM images (Fig. 9b, c) show the morphology of the coating. A WCA of 153° was measured, and the authors reported that temperature fluctuations affect hydrophobicity, increasing it with increasing temperature and decreasing it when cooled (Fig. 9d, e). This behavior is linked to the molecular dynamics of PDMS and SiO_2. In PDMS, lower temperatures reduce molecular motion, aligning methyl side chains and smoothing surfaces, which decreases hydrophobicity. Higher temperatures enhance molecular activity, improving water repellency. Similarly, in SiO_2, increased temperatures weaken hydrogen bonds between water molecules, enhancing its hydrophobic properties. To evaluate the electrothermal properties of the coating,

Table 4 The summary of the combination of photo/electrothermal and superhydrophobic strategies

Category	Ref	Publication year	Composition	MXene loading	Type of composite/thickness	WCA (°)/SA (°)	Heat source/photothermal properties	Electrothermal properties	Ice adhesion	Delayed icing time
Combination of photo/electrothermal and superhydrophobic strategies	[13]	2022	$Ti_3C_2T_x$@PTFE@ND (nanodiamond)	25 wt%	Layered film/NR	160.18/1.8	Xenon lamp/54.9 °C at 100 mW cm^{-2} in 120 s	NR	56.4 kPa	76 s at 100 mW cm^{-2}, at − 20 °C, RH 35%
	[64]	2022	$fSiO_2$/$Ti_3C_2T_x$@Au-WPU	NR	Film/NR	153/4.5	NIR/120 °C at 500 mW cm^{-2}	NR	NR	1053 s at − 20 °C, RH 68%
	[65]	2022	Polyurethane urea polymer/AgNW/ZnO/flourinated $Ti_3C_2T_x$	NR	Film/NR	156.5/NR	NIR laser/40, 51.6, 73.3 °C, at 8, 1.2, 1.6 W in 300 s	NR	8.4 kPa	210 s
	[66]	2023	$Ti_3C_2T_x$@PPy/PDMS	NR	Fabric/362.9 µm	152/7	NR	40.1, 66.3, 98.9, 145.2 °C at 4, 6, 8, and 10 V in 5 min	NR	NR
	[67]	2023	$Ti_3C_2T_x$/PEI	5 wt%	Film/40 µm	157/7	NIR light/20 °C to 90 °C in 10 s, 188 °C in 50 s	NR	82 kPa	127 s at − 20 °C, RH 30%
	[68]	2024	Melamine spong@PVA-$Ti_3C_2T_x$-PDA@lignine particles	NR	Aerogel/NR	152.3/6	Artificial sunlight/56 °C at 100 mW cm^{-2}	NR	NR	NR
	[69]	2024	PDMS/Ni@$Ti_3C_2T_x$	NR	Film/NR	154.7/3.8	NR/52.8, 85, 91.5 °C at 50, 100, 125 mW cm^{-2}	NR	4.7 kPa	NR
	[70]	2024	Fluorinated $Ti_3C_2T_x$, hydrophobic SiO_2 NPs, epoxy, PDMS	5 w%	Film/237 µm	158/4	Xenon lamp/75.9 °C at 100 mW cm^{-2}	NR	15 kPa	450 s, 256 s, 122 s at substrate temperature of − 10 °C, − 20 °C, − 30 °C, RH 80%

Table 4 (continued)

Category	Ref	Publication year	Composition	MXene loading	Type of composite/thickness	WCA (°)/SA (°)	Heat source/photothermal properties	Electrothermal properties	Ice adhesion	Delayed icing time
	[71]	2024	N-Boroxine-PDMS/SiO_2@$Ti_3C_2T_x$/AgNWs	NR	Layered film/NR	153/NR	Sunlight/56 °C at 100 mW cm^{-2}	36.3, 54.1, 60.6 °C, at 1.5, 3, 5 V	NR	NR
	[72]	2024	Melamine spong@PDA/lignine@$Ti_3C_2T_x$	NR	Sponge/NR	153.7/3	Artificial sunlight/62.8 °C at 100 mW cm^{-2} in 200 s	NR	NR	650 s, 298 s, 178 s at − 5, − 15, − 25 °C

NR Not reported

when voltages of 1.5, 3, and 5 V were applied, the temperature increased to 36.3, 54.1, and 60.6 °C, respectively. Under the irradiation at 50 and 100 mW cm^{-2} stabilized temperatures of 40 and 56 °C were recorded.

A superhydrophobic fabric was decorated with $Ti_3C_2T_x$ and the in situ growth of polypyrrole was followed by a PDMS coating [66]. Within 5 min of applying 4, 6, 8, and 10 V across the fabric, the surface temperature reached 40.1, 66.3, 98.9, and 145.2 °C, respectively. When an ice cube from 350 µL of water was placed on a 15° tilted fabric at room temperature, it started to melt and roll off after 80 s of applying 8 V, whereas it barely melted after 380 s in the absence of voltage. The WCA of the fabric remained constant at different pH values, ultrasonic treatment for up to 180 min, irradiation for up to 300 min, and even bending after 500 cycles.

In one study [69], a magnetic field was used to introduce a specific structure to the coating. Magnetic Ni@$Ti_3C_2T_x$ was spray-coated on an Al foil while it was placed on a strong magnet to obtain a self-assembled eyelash-like microstructure array before being coated with PDMS as a hydrophobic agent/binder and surface protector [69]. The surface with multiscale roughness, with a WCA of 154.7° and an SA of 3.8°, showed self-cleaning properties even when the melted ice washed away dust and other pollutants. As the solar energy density increased to 50, 100, and 125 mW cm^{-2}, the surface temperature reached 52.8, 85, and 91.5 °C, respectively. Under 100 mW cm^{-2} a 4-mm-thick ice cube melted in 558 s, while the film developed in the absence of the magnetic field, took 604 s. For the surface fabricated in the presence and absence of a magnetic field, the ice formation was delayed to 73 s and 31 s, respectively, and ice adhesion strength of 4.7 and 52.7 kPa, respectively, were observed. When the film was exposed to high humidity, sunlight, and spray test in a Xenon lamp aging weathering chamber for 10 days, it showed high durability. After 40 cycles of particle aberration and acid washing, the WCA remained above 150° and the SA below 10°, indicating that the microarray structure stayed relatively intact.

Inspired by lotus leaves and human skin, Zhang et al. [65] fabricated a rather transparent multifunctional superhydrophobic film via LBL spray–coating of AgNWs, ZnO NPs, and fluorinated $Ti_3C_2T_x$ on a polyurethane urea–based self-healing polymer substrate. The original WCA of 156.5° was reported to be constant after 100 sand flow cycles, a scotch tape test, 6 h in NaOH solution, and 24 h in HCl solution. When exposed to NIR laser at powers of 8, 1.2, and 1.6 W, the surface temperature increased to 40, 51.6, and 73.3 °C, respectively, in 300 s. The ice adhesion strength of the uncoated film (41.6 kPa) significantly decreased to 8.4 kPa after the MXene-based coating and icing were applied, which was delayed to 210 s. An incompletely melted freezing droplet slid off the surface after 30 s of irradiation at

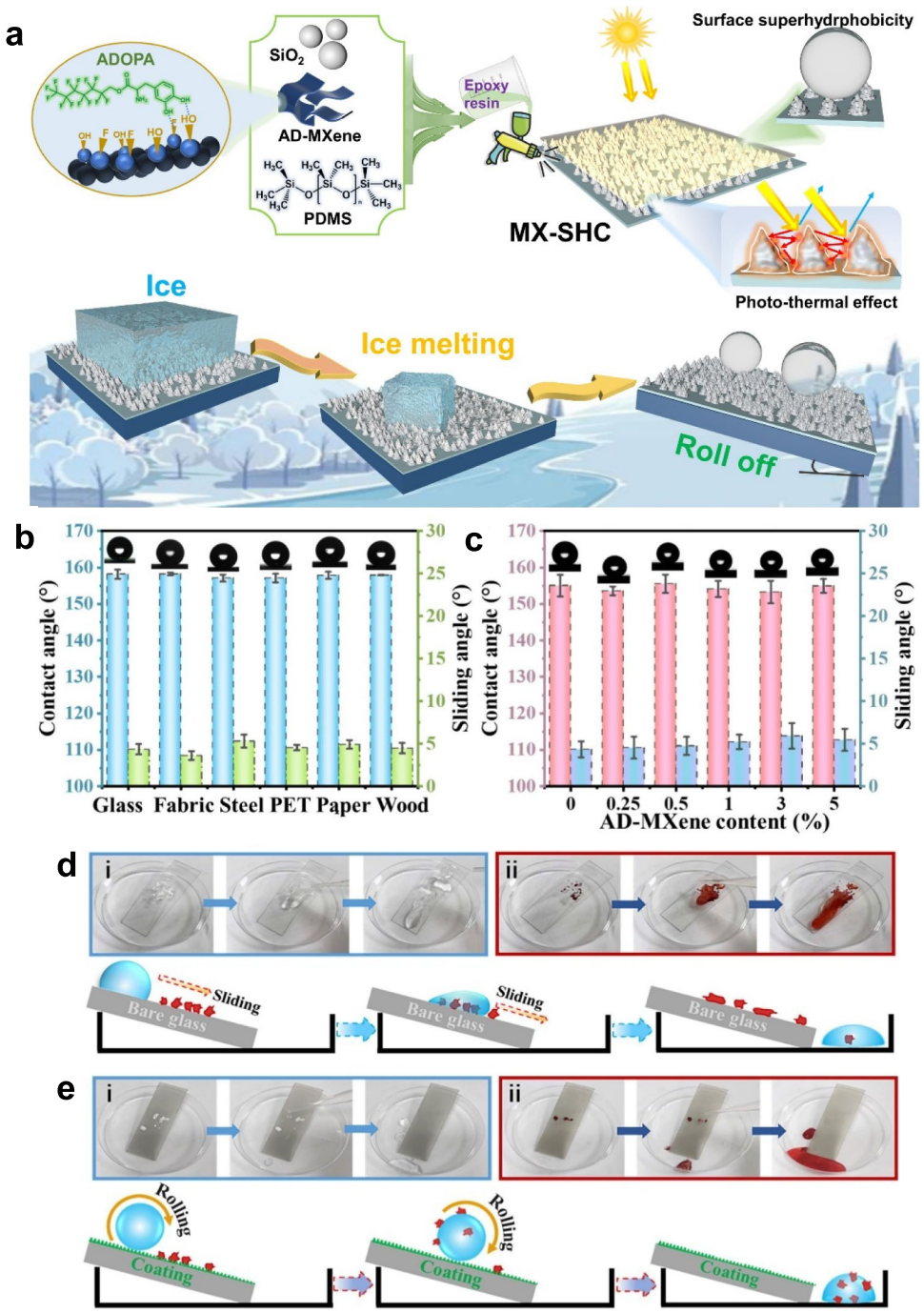

Fig. 8 **a** Schematic illustration of the preparation process and design concept of fluorinated MXene–doped superhydrophobic coatings (MX–SHCs). **b** WCAs and SAs on MX–SHCs prepared on different substrates. **c** Effect of the AD–MXene content on surface wettability of MX–SHC. Investigation of the self-cleaning ability of MX–SHC. **d** Removal of dye contaminants on pristine glass by dripping water. **e** Removal of dye contaminants on MX–SHC sample by dripping water. Reproduced with permission from Elsevier [70]

1.6 W, reducing the risk of secondary icing. This durable structure is suitable for protecting solar panels from icing while maximizing light absorption efficiency.

The melamine sponge (MS) was decorated with lignin particles (LPs)@$Ti_3C_2T_x$ via the impregnation method and self-polymerized dopamine (PDA) to obtain MS@PDA/LPs@MXene [68] which was subsequently modified with a fluorine-containing low surface energy material. PDA was used to improve the adhesion between MXene and LPs. The superhydrophobic sponge (WCA = 153.7°, SA = 3°) showed self-cleaning and oil-absorbing properties. Under 100 mW cm^{-2} irradiation the temperature of the pristine MS reached 26.7 °C, MS@PDA to 53.5 °C, and MS@PDA/LPs@MXene to 58.6 °C within 30 s. MS@PDA/LPs@MXene showed a temperature increase to 47.5, 62.8, 72.6, and 93.8 °C at 50, 100, 150, 200 mW cm^{-2} in 200 s, illustrating the effect of MXene. The icing delay of 20-μL water droplet on the MS@PDA/LPs@MXene was 650, 298, and 178 s when the temperature of the substrates was − 5, − 15, and − 25 °C, respectively. The surface remained ice-free at − 17.9 °C and

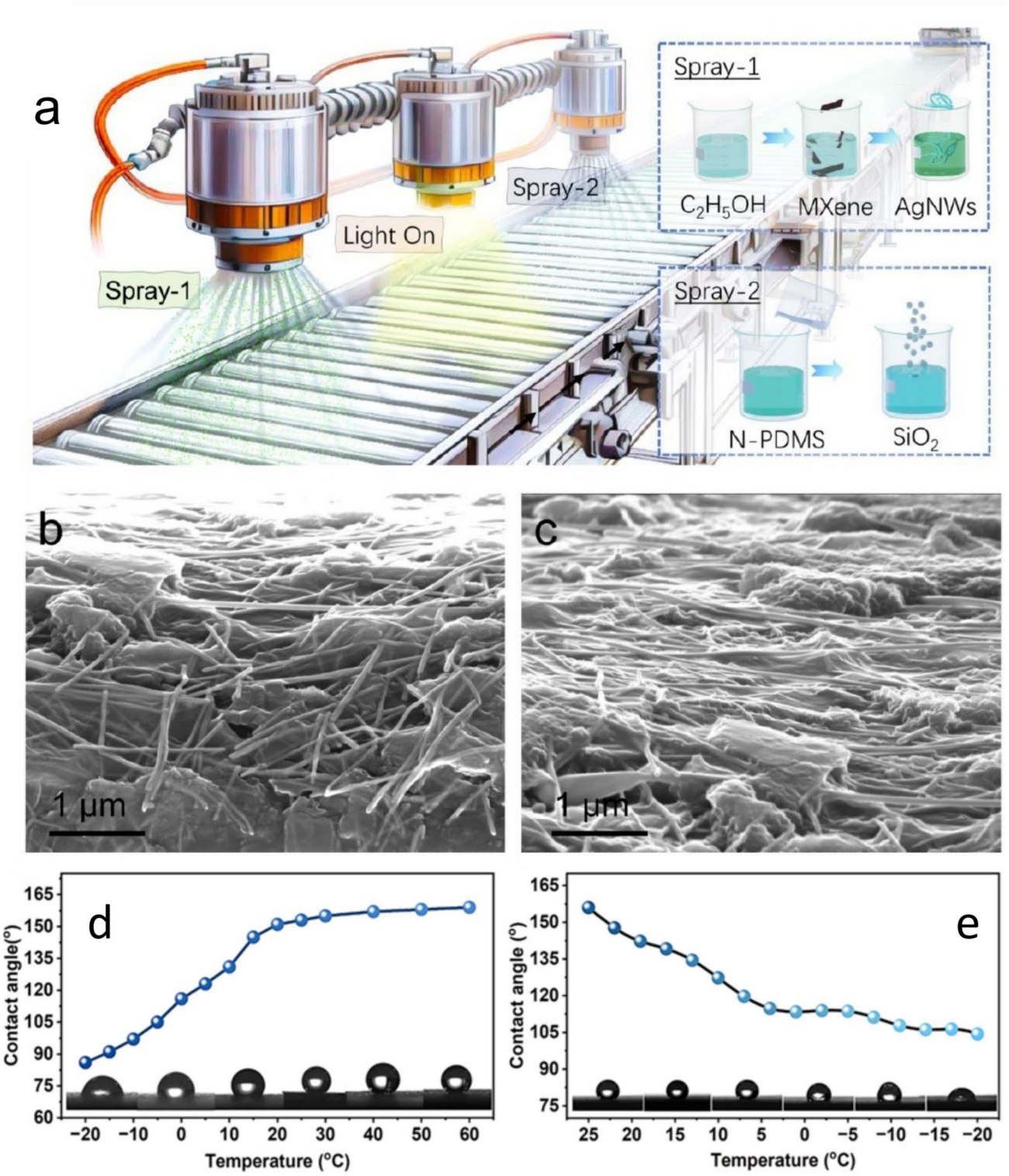

Fig. 9 **a** Schematic illustration of the preparation process and **b**, **c** SEM images of $Ti_3C_2T_x$/AgNWs/N–boroxine–PDMS/SiO_2. **d** Hydrophobicity test results during heating and **e** cooling processes. Reproduced with permission from ACS [71]

RH = 90% under 50 mW cm^{-2}. It took 143 s for MS@PDA/LPs@MXene under 100 mW cm^{-2} and 560 s for MS to melt an ice droplet, which was attributed to the synergistic photothermal effects of PDA and LPs@MXene. The same group [72] reported an MS sponge composite with a slight difference in fabrication, in which they dipped the sponge in

PVA to enhance the adhesion between MXene and melamine before proceeding with the rest of the coating as Wang et al. [68] to obtain the MS@PVA-MXene-PDA@LP sponge. Its surface temperature reached 42.2, 56, 67.6, and 84 °C at 50, 100, 150, and 200 mW cm^{-2}, respectively, in 200 s, showing a slight decrease compared to that of MS@PDA/LPs@MXene. They tested the melting of a 100-µL droplet at − 18 °C, which was 440 s under 100 mW cm^{-2}. The anti-corrosion characteristics of MS@PDA/LPs@MXene were tested by coating a NdFeB magnet with this composite, which resulted in a corrosion current density approximately one order of magnitude lower than that of bare NdFeB in a 5-g L^{-1} NaCl solution.

Xue et al. [67] fabricated a superhydrophobic film (40 µm) by curing $Ti_3C_2T_x$ and PEI mixture and subsequently laser etching to create micropillars. With 5 wt% MXene loading amount, the film had a WCA of 157° and an SA of 7°, an ice adhesion strength of 82 kPa, and an icing delay of 127 s at − 20 °C and RH = 30%. Under low-power NIR light, the temperature of the film increased from 20 to 90 °C within 10 s, and to 188 °C within 50 s, and an ice droplet melted within 19 s. Zhao et al. [13] developed a layered film via calcination of $Ti_3C_2T_x$, PTFE, and nanodiamond (MXene@PTFE@ND). With WCA = 160.18°, SA = 1.8°, at 100 mW cm^{-2} the surface temperature of 20 °C reached 43.4, 54,9, and 109.3 °C in 30, 120, and 360 s, respectively. An ice droplet placed over the coating was melted in 76 s under 100 mW cm^{-2} while it took 120 s in the absence of MXene (PTFE@ND). The ice adhesion strengths of 56.4 and 98.3 kPa and freezing times of 403 s and 184 s were obtained for MXene@PTFE@ND and PTFE@ND, respectively. The reasons for this can be as follows: (1) greater surface roughness and a reduced contact area, (2) lower thermal conductivity, and (3) less heat transfer in MXene@PTFE@ND.

7 Conclusion and challenges

Icing is an unavoidable phenomenon in nature. Next-generation coatings are best designed to possess passive anti-icing and active deicing properties by (1) lowering ice adhesion strength, (2) rapidly melting ice via electro and photothermal techniques. The development of multifunctional MXene-based superhydrophobic surfaces has shown remarkable potential in meeting these criteria. This review summarizes the design strategies for fabricating MXene-based nanocomposites that leverage their electro and photothermal characteristics.

The key findings from this review include the following:

1. MXenes are excellent electro/photothermal 2D materials because of their localized surface plasmon resonance (LSPR) for photothermal conversion, high electrical conductivity for Joule heating, and thermal stability.
2. Hybridization with different nanomaterials, such as AgNWs, graphene, SiO_2 NPs, Au NPs, and polymers such as PDA, PDMS, PU, and PI, significantly improves conductivity, structural stability, superhydrophobicity, heat transfer, durability, and oxidation resistance.
3. The fabrication methods optimize the coating performance. LBL assembly by spray-coating and VAF enables large-scale production and enhances properties. Aerogels are lightweight and flexible, exhibit reduced thermal loss, and optimized MXene dispersion for enhanced heat transfer. Surface patterning introduces micro/nanoroughness for superhydrophobicity and self-cleaning. Self-healing polymer matrices improve mechanical robustness.
4. MXene is a promising material in low-voltage systems. The primary goal is to use a minimal amount of electrical power to generate sufficient heat for deicing. For MXene, this is particularly relevant due to its high electrical conductivity. Many studies have shown that MXene-based coating can melt the ice with a voltage of 2.5 V rather than the much higher voltages required by traditional systems. This can be easily powered by accessible and safe power sources such as batteries, solar panels, and standard DC power supplies.
5. The outdoor durability of a coating is an important parameter for its long-term practical application. To simulate real-world conditions, MXene-based composites were exposed to multi-faceted testing regimens such as mechanical abrasion using sand impact test and scotch tape test, as well as chemical and environmental stability tests like corrosive solutions, extreme heat, and cold.

Despite their remarkable performance, there are challenges and limitations in designing MXene-based anti-icing and deicing coatings. MXene oxidizes in humid and oxygen-rich environments, degrading conductivity and photothermal properties. Fluorination and PDMS encapsulation improve stability but may reduce electrical performance. Thus, balancing these two important factors is highly important. Superhydrophobic coatings work well; however, they degrade over time due to mechanical abrasion and environmental exposure. Secondary freezing after the initial melting remains challenging, especially in high-humidity environments. Lowering ice adhesion strength requires low-energy materials, which mostly contain fluorine and are considered not environmentally friendly. With respect to electric power consumption, optimizing MXene conductivity and using hybrid solar-electrothermal heating systems could improve sustainability. Large-scale and manufacturing costs require developing green synthesis methods for MXene production and optimizing coating. The synthesis and processing of

MXenes are complex and expensive. Designing coatings for real-world applications requires optimizing fabrication techniques, e.g., spray-coating, dip-coating, and 3D printing. Even though hierarchical porous structures exhibit high efficiency, scalability is still challenging.

Harnessing the tools of artificial intelligence (AI) for boosting innovation in functional materials design and engineering, as well as discovering new materials for targeted applications, is revolutionizing the field of materials science. AI-driven approaches, such as machine learning (ML), high-throughput screening, and computational modeling, enable the rapid prediction of material properties, phase stability, and performance optimization, significantly reducing experimental costs and time. By leveraging big data analytics and autonomous material discovery, AI facilitates the design of next-generation MXene-based coatings with enhanced anti-icing, deicing, and self-healing properties, accelerating the transition from laboratory research to real-world applications.

Overall, with advances in material synthesis, fabrication, and energy-efficient design, MXene-based coatings have the potential to revolutionize anti-icing and deicing applications in aviation, automotive, renewable energy, and wearable electronics.

Author contribution ABA participated in draft preparation, figure preparation and permission acquisition. MN conceptualized the subject, wrote and reviewed the draft, and acquired the funding. Both authors contributed to responding to reviewers' comments.

Funding This work was financially supported by the FLAG-ERA grant [GRAPH-OCD], by the Scientific and Technological Research Council of Turkey (TUBITAK) [223N171].

Data availability No datasets were generated or analysed during the current study.

Declarations

Competing interests The authors declare no competing interests.

Open Access This article is licensed under a Creative Commons Attribution-NonCommercial-NoDerivatives 4.0 International License, which permits any non-commercial use, sharing, distribution and reproduction in any medium or format, as long as you give appropriate credit to the original author(s) and the source, provide a link to the Creative Commons licence, and indicate if you modified the licensed material. You do not have permission under this licence to share adapted material derived from this article or parts of it. The images or other third party material in this article are included in the article's Creative Commons licence, unless indicated otherwise in a credit line to the material. If material is not included in the article's Creative Commons licence and your intended use is not permitted by statutory regulation or exceeds the permitted use, you will need to obtain permission directly from the copyright holder. To view a copy of this licence, visit http://creativecommons.org/licenses/by-nc-nd/4.0/.

References

1. Zhou L, Liu R, Yi X (2022) Research and development of anti-icing/deicing techniques for vessels: review. Ocean Eng 260:112008. https://doi.org/10.1016/j.oceaneng.2022.112008
2. Li B, Bai J, He J, Ding C, Dai X, Ci W et al (2023) A review on superhydrophobic surface with anti-icing properties in overhead transmission lines. Coatings 13(2):301. https://doi.org/10.3390/coatings13020301
3. Liu L, Tang W, Ruan Q, Wu Z, Yang C, Cui S et al (2020) Robust and durable surperhydrophobic F-DLC coating for anti-icing in aircrafts engineering. Surf Coat Technol 404:126468. https://doi.org/10.1016/j.surfcoat.2020.126468
4. Parent O, Ilinca A (2011) Anti-icing and de-icing techniques for wind turbines: critical review. Cold Reg Sci Technol 65(1):88–96. https://doi.org/10.1016/j.coldregions.2010.01.005
5. Zhang Y, Liu Z, Shi X (2021) Development and use of salt-storage additives in asphalt pavement for anti-icing: literature review. J Transp Eng, Part B: Pavements 147(4):03121002. https://doi.org/10.1061/JPEODX.0000311
6. Zhou H, Xu Q, Zhao J, Luo H, Huang X, Huang J (2023) Biomimetic super slippery surface with excellent and durable anti-icing property for immovable heritage conservation. Prog Org Coat 184:107818. https://doi.org/10.1016/j.porgcoat.2023.107818
7. Alves DF, Sousa JPS (2024) Fluorine-free approaches to impart photovoltaic systems with self-cleaning and anti-icing features. J Coat Technol Res 21(6):1907–1919. https://doi.org/10.1007/s11998-024-00936-1
8. Chen Q, Yin X, You D, Hou H, Tong G, Wang B et al (2009) Review on blackout process in China Southern area main power grid in 2008 snow disaster. In: 2009 IEEE Power & Energy Society General Meeting, pp 1–8. https://doi.org/10.1109/PES.2009.5275700
9. Wang F, Zhuo Y, He Z, Xiao S, He J, Zhang Z (2021) Dynamic anti-icing surfaces (DAIS). Adv Sci 8(21):2101163. https://doi.org/10.1002/advs.202101163
10. Azimi Yancheshme A, Allahdini A, Maghsoudi K, Jafari R, Momen G (2020) Potential anti-icing applications of encapsulated phase change material–embedded coatings; a review. J Energy Storage 31:101638. https://doi.org/10.1016/j.est.2020.101638
11. https://www.statsandresearch.com/report/11664-global-full-ice-protection-system-fips-sales-market/. Accessed 21 Feb 2025
12. He Z, Xie H, Jamil MI, Li T, Zhang Q (2022) Electro-/photothermal promoted anti-icing materials: a new strategy combined with passive anti-icing and active de-icing. Adv Mater Interfaces 9(16):2200275. https://doi.org/10.1002/admi.202200275
13. Zhao Y, Yan C, Hou T, Dou H, Shen H (2022) Multifunctional Ti3C2Tx MXene-based composite coatings with superhydrophobic anti-icing and photothermal deicing properties. ACS Appl Mater Interfaces 14(22):26077–26087. https://doi.org/10.1021/acsami.2c07087
14. Li Z, Lei H, Kan A, Xie H, Yu W (2021) Photothermal applications based on graphene and its derivatives: a state-of-the-art review. Energy 216:119262. https://doi.org/10.1016/j.energy.2020.119262
15. Zhang H, Guo H, Jiang R, Wan W, Deng P, Zhou X (2024) Research progress of multifunctional anti-icing composites materials. J Appl Polym Sci 141(36):e55922. https://doi.org/10.1002/app.55922
16. Tan KW, Yap CM, Zheng Z, Haw CY, Khiew PS, Chiu WS (2022) State-of-the-art advances, development, and challenges of metal oxide semiconductor nanomaterials for photothermal solar steam generation. Adv Sustain Syst 6(4):2100416. https://doi.org/10.1002/adsu.202100416

17. Zeng W, Ye X, Dong Y, Zhang Y, Sun C, Zhang T et al (2024) Mxene for photocatalysis and photothermal conversion: synthesis, physicochemical properties, and applications. Coord Chem Rev 508:215753. https://doi.org/10.1016/j.ccr.2024.215753
18. Shi Y, Wang Y, Meng N, Liao Y (2024) Photothermal conversion porous organic polymers: design, synthesis, and applications. Small Methods 8(10):2301554. https://doi.org/10.1002/smtd.202301554
19. Xu D, Li Z, Li L, Wang J (2020) Insights into the photothermal conversion of 2D MXene nanomaterials: synthesis, mechanism, and applications. Adv Funct Mater 30(47):2000712. https://doi.org/10.1002/adfm.202000712
20. Altan A, Namvari M (2023) Multifunctional, flexible, and mechanically robust polyimide-MXene nanocomposites: a review. 2D Mater 10(4):042001. https://doi.org/10.1088/2053-1583/acf327
21. Namvari M, Chakrabarti BK (2024) Electrophoretic deposition of MXenes and their composites: toward a scalable approach. Adv Colloid Interface Sci 331:103208. https://doi.org/10.1016/j.cis.2024.103208
22. Zahrabi M, Altunbek M, Celik S, Namvari M, Koc B (2025) 3D melt electrowritten MXene-reinforced scaffolds for tissue engineering applications. Biofabrication. https://doi.org/10.1088/1758-5090/adf803
23. Lim KRG, Shekhirev M, Wyatt BC, Anasori B, Gogotsi Y, Seh ZW (2022) Fundamentals of MXene synthesis. Nature Synthesis 1(8):601–614. https://doi.org/10.1038/s44160-022-00104-6
24. Fan X, Liu L, Jin X, Wang W, Zhang S, Tang B (2019) MXene Ti3C2Tx for phase change composite with superior photothermal storage capability. J Mater Chem A 7(23):14319–14327. https://doi.org/10.1039/C9TA03962G
25. Kabir L, Qi J, Wijaya K, Sagadevan S, Yoon C-M, Ullah K et al (2024) Recent advances and latest technologies in energy storage applications based on 2D MXene. J Energy Storage 80:110335. https://doi.org/10.1016/j.est.2023.110335
26. Qin R, Nong J, Wang K, Liu Y, Zhou S, Hu M et al (2024) Recent advances in flexible pressure sensors based on MXene materials. Adv Mater 36(24):2312761. https://doi.org/10.1002/adma.202312761
27. Namvari M, Inan T, Altan A (2023) MXene-cellulose nanofiber composites: toward green, multi-functional, flexible, and highly efficient electromagnetic interference shielding materials. Graphene and 2D Mater 8(1):5–26. https://doi.org/10.1007/s41127-023-00056-4
28. Maleki A, Ghomi M, Nikfarjam N, Akbari M, Sharifi E, Shahbazi M-A et al (2022) Biomedical applications of MXene-integrated composites: regenerative medicine, infection therapy, cancer treatment, and biosensing. Adv Funct Mater 32(34):2203430. https://doi.org/10.1002/adfm.202203430
29. Lin H, Gao S, Dai C, Chen Y, Shi J (2017) A two-dimensional biodegradable niobium carbide (MXene) for photothermal tumor eradication in NIR-I and NIR-II biowindows. J Am Chem Soc 139(45):16235–16247. https://doi.org/10.1021/jacs.7b07818
30. Li N, Wang Y, Li Y, Zhang C, Fang G (2024) Recent advances in photothermal therapy at near-infrared-II based on 2D MXenes. Small 20(6):2305645. https://doi.org/10.1002/smll.202305645
31. Zada S, Dai W, Kai Z, Lu H, Meng X, Zhang Y et al (2020) Algae extraction controllable delamination of vanadium carbide nanosheets with enhanced near-infrared photothermal performance. Angew Chem Int Ed 59(16):6601–6606. https://doi.org/10.1002/anie.201916748
32. Kumar Deb S, Dutta P, Masud Karim G, Patra A, Bera P, Das S et al (2024) Bulk versus surface-limited polymer encapsulation: a current pulse-induced approach for confined polymer coating selectively over quasi-oriented MXene aerogel. Chem Eng J 484:149617. https://doi.org/10.1016/j.cej.2024.149617
33. Hu F, Li M, Li P, Zeng J, Wang T, Li J et al (2025) High-performance multifunctional nanopapers with superior mechanical strength, electromagnetic interference shielding, and thermal management for next-generation electronics. Adv Funct Mater 35(17):2418899. https://doi.org/10.1002/adfm.202418899
34. Zhang R, Yang Y, Zhang H, Ma X, Li J (2024) 3D liquid-based porous coating integrated with oleophilic MXene nanoflakes for durable ultra-low ice adhesion and exceptional photothermal slippery properties. Chem Eng J 496:154108. https://doi.org/10.1016/j.cej.2024.154108
35. Song X, Hou Z, Gan Z, Hu Y, Zheng H, Wu Y et al (2024) Biomimetic lubricant-grafted surfaces on laser-textured microwell arrays with multifunctionality. Friction 12(12):2707–2725. https://doi.org/10.1007/s40544-024-0906-3
36. Niu W, Chen GY, Xu H, Liu X, Sun J (2022) Highly transparent and self-healable solar thermal anti-/deicing surfaces: when ultrathin MXene multilayers marry a solid slippery self-cleaning coating. Adv Mater 34(10):2108232. https://doi.org/10.1002/adma.202108232
37. Cai W, Li Z, Cui T, Feng X, Song L, Hu Y et al (2022) Self-assembly of hierarchical MXene@SnO2 nanostructure for enhancing the flame retardancy, solar de-icing, and mechanical property of polyurethane resin. Compos Part B Eng 244:110204. https://doi.org/10.1016/j.compositesb.2022.110204
38. Su F, Xie J, Li X, He Z, Wang H, Zhang J et al (2023) Electrostatically assisted construction modified MXene-IL-based nanofluids for photothermal conversion. ACS Appl Mater Interfaces 15(11):14316–14328. https://doi.org/10.1021/acsami.2c22517
39. Cui T, Cai W, Zheng Y, Wang J, Lin B, Gui Z et al (2023) Unlocking interfacial dynamics of biocompatible MXene/polyurethane-based nanocomposites for photothermal de-icing and thermal safety. Chem Eng J 473:145357. https://doi.org/10.1016/j.cej.2023.145357
40. Su F, He Z, Xie J, Zhang J, Zhang W, Xin Y et al (2023) Ti3C2Tx and copper sulfide composite nanofluids with a hierarchical structure for sustainable and efficient solar light–thermal conversion. J Mater Chem A 11(38):20651–20664. https://doi.org/10.1039/D3TA03908K
41. Liu Z, Wu F, Lv T, Qu Y, Zhang Z, Yu C et al (2024) Ti3C2TX/carbon aerogels derived from winter melon for high-efficiency photothermal conversion. Desalination 573:117207. https://doi.org/10.1016/j.desal.2023.117207
42. He Z, Zhang W, Zhang J, Xie J, Su F, Li Y et al (2024) Enhancing the electromagnetic interference shielding of epoxy resin composites with hierarchically structured MXene/graphene aerogel. Compos Part B Eng 274:111230. https://doi.org/10.1016/j.compositesb.2024.111230
43. Zheng S, Xu W, Liu J, Pan F, Zhao S, Wang Y et al (2024) One-hour ambient-pressure-dried, scalable, stretchable MXene/polyurea aerogel enables synergistic defense against high-frequency mechanical shock and electromagnetic waves. Adv Funct Mater 34(38):2402889. https://doi.org/10.1002/adfm.202402889
44. Yang P, Xia T, Ghosh S, Wang J, Rawson SD, Withers PJ et al (2021) Realization of 3D epoxy resin/Ti3C2Tx MXene aerogel composites for low-voltage electrothermal heating. 2D Mater 8(2):025022. https://doi.org/10.1088/2053-1583/abda0f
45. Gao Q, Pan Y, Zheng G, Liu C, Shen C, Liu X (2021) Flexible multilayered MXene/thermoplastic polyurethane films with excellent electromagnetic interference shielding, thermal conductivity, and management performances. Adv Compos Hybrid Mater 4(2):274–285. https://doi.org/10.1007/s42114-021-00221-4
46. Sun K, Wang F, Yang W, Liu H, Pan C, Guo Z et al (2021) Flexible conductive polyimide fiber/MXene composite film for electromagnetic interference shielding and joule heating with excellent harsh environment tolerance. ACS Appl Mater Interfaces 13(42):50368–50380. https://doi.org/10.1021/acsami.1c15467

47. Monastyreckis G, Siles JT, Knotek P, Omastova M, Aniskevich A, Zeleniakiene D (2022) Scalable MXene and PEDOT-CNT nanocoatings for fibre-reinforced composite de-icing. Materials 15(10):3535
48. Ran L, Qiu L, Sun F, Chen Z, Zhao L, Yi L et al (2023) Multilayer assembly of strong and tough MXene/cellulose films for excellent electromagnetic shielding. J Alloys Compd 961:171020. https://doi.org/10.1016/j.jallcom.2023.171020
49. Ran L, Qiu L, Zhao H, Sun F, Chen Z, Zhao L et al (2023) Fabrication of MXene based sandwich-like films for excellent flexibility, electromagnetic interference shielding and thermal management. Compos Part A Appl Sci Manuf 173:107672. https://doi.org/10.1016/j.compositesa.2023.107672
50. Hu Y, Yang G, Chen J, Li Y, Dong M, Zhang H et al (2024) Interfacial engineering of hybrid MXene-Ni-CF tri-core–shell composites for electromagnetic interference shielding and E-heating applications. Compos Part A Appl Sci Manuf 178:107990. https://doi.org/10.1016/j.compositesa.2023.107990
51. Liu J, Zhang L, Zhao H, Zhang Z (2024) Highly transparent MXene/silver nanowire conductors for high-performance transparent heater. Opt Mater 153:115575. https://doi.org/10.1016/j.optmat.2024.115575
52. Zhang J, Zhang L, Lv C, Gao L, Chen X, Luo S et al (2024) Lightweight, ultra-strength, multifunctional MXene/wood composite film designed by densification strategy for electrode, thermal management, and electromagnetic shielding application. Ind Crops Prod 216:118700. https://doi.org/10.1016/j.indcrop.2024.118700
53. Ma Z, He J, Liu S, Qie X, Gan M, Cheng R et al (2024) Gradient layered MXene/Fe3O4@CNTs/TOCNF ultrathin nanocomposite paper exhibiting effective electromagnetic shielding and multifunctionality. Nano Res 17(9):8233–8242. https://doi.org/10.1007/s12274-024-6824-x
54. Xia Z, Zhang T, Tian L, Tian B, Ni J, Hou F et al (2024) Flexible MXene hybrid films with a tuned silver nanowire framework for electromagnetic interference shielding and ultralow voltage-driven joule heating. ACS Appl Nano Mater 7(4):3748–3760. https://doi.org/10.1021/acsanm.3c05342
55. Park TH, Yu S, Koo M, Kim H, Kim EH, Park J-E et al (2019) Shape-adaptable 2D titanium carbide (MXene) heater. ACS Nano 13(6):6835–6844. https://doi.org/10.1021/acsnano.9b01602
56. Li S, Zhang J, He J, Liu W, Wang Y, Huang Z et al (2023) Functional PDMS elastomers: bulk composites, surface engineering, and precision fabrication. Adv Sci 10(34):2304506. https://doi.org/10.1002/advs.202304506
57. Qin W, Lin C, Geng J, Xue Y, Zhong M, Zou Y et al (2022) Multifunctional MXene/CNT-based layered film for icing detection, anti-icing, and deicing application. Ceram Int 48(22):32767–32776. https://doi.org/10.1016/j.ceramint.2022.07.201
58. Li B, Yang Y, Wu N, Zhao S, Jin H, Wang G et al (2022) Bicontinuous, high-strength, and multifunctional chemical-cross-linked MXene/superaligned carbon nanotube film. ACS Nano 16(11):19293–19304. https://doi.org/10.1021/acsnano.2c08678
59. Zhou Z, Song Q, Huang B, Feng S, Lu C (2021) Facile fabrication of densely packed Ti3C2 MXene/nanocellulose composite films for enhancing electromagnetic interference shielding and electro-/photothermal performance. ACS Nano 15(7):12405–12417. https://doi.org/10.1021/acsnano.1c04526
60. Li B, Wu N, Yang Y, Pan F, Wang C, Wang G et al (2023) Graphene oxide-assisted multiple cross-linking of MXene for large-area, high-strength, oxidation-resistant, and multifunctional films. Adv Funct Mater 33(11):2213357. https://doi.org/10.1002/adfm.202213357
61. Liu Z, Zhang J, Zhao Yn, Wu F, Lv T, Yu L et al (2024) Ta4C3TX/graphene aerogels with combined photo/electro-thermal conversion performances for multifunctional applications. Chem Eng J 489:151196. https://doi.org/10.1016/j.cej.2024.151196
62. Zhang Y, Guo Z (2024) Dual-drive energy conversion plasmonic Ag@MXene thermal management textiles inspired by bearing structure. Chem Eng J 493:152587. https://doi.org/10.1016/j.cej.2024.152587
63. Hu F, Li M, Li P, Zeng J, Wang T, Li J et al (2025) High-performance multifunctional nanopapers with superior mechanical strength, electromagnetic interference shielding, and thermal management for next-generation electronics. Adv Funct Mater. https://doi.org/10.1002/adfm.202418899
64. Wang J, Li P, Yu P, Leydecker T, Bayer IS, Losic D et al (2022) Efficient photothermal deicing employing superhydrophobic plasmonic MXene composites. Adv Compos Hybrid Mater 5(4):3035–3044. https://doi.org/10.1007/s42114-022-00549-5
65. Zhang L, Zhang H, Yu X, Xu L, Wang D, Lu X et al (2022) Superhydrophobic MXene coating with biomimetic structure for self-healing photothermal deicing and photoelectric detector. ACS Appl Mater Interfaces 14(47):53298–53313. https://doi.org/10.1021/acsami.2c16111
66. He H, Guo Z (2023) Fabric-based superhydrophobic MXene@polypyrrole heater with superior dual-driving energy conversion. J Colloid Interface Sci 629:508–521. https://doi.org/10.1016/j.jcis.2022.08.176
67. Xue Y, Wang Y, Sui X, Liang W, Wang F (2023) Superhydrophobic, photothermal, MXene/PEI composite film with anti-icing and deicing properties. Mater Lett 347:134638. https://doi.org/10.1016/j.matlet.2023.134638
68. Wang M, Zhou Z, Qiao L, Lin B, He Z (2024) Facile preparation of photothermal and superhydrophobic melamine sponge for oil/water separation and anti-icing. J Environ Chem Eng 12(6):114393. https://doi.org/10.1016/j.jece.2024.114393
69. Chen J, Chen X, Hao Z, Wu Z, Selim MS, Yu J et al (2024) Robust and superhydrophobic polydimethylsiloxane/Ni@Ti3C2Tx nanocomposite coatings with assembled eyelash-like microstructure array: a new approach for effective passive anti-icing and active photothermal deicing. ACS Appl Mater Interfaces 16(20):26713–26732. https://doi.org/10.1021/acsami.4c01561
70. Zhang J, Zhang P, Hu Z, Li C, Cui X, Yan B (2024) A fluorinated MXene-doped superhydrophobic coating with mechanochemical robustness, repairable wettability and photothermal conversion for highly efficient anti/de-icing. Chem Eng J 498:155499. https://doi.org/10.1016/j.cej.2024.155499
71. Cui T, Ang EH, Zheng Y, Cai W, Wang J, Hu Y et al (2024) Ultrahigh transparent safety film for spectrally selective photo/electrothermal conversion via surface-enhanced plasma resonance dynamics. Nano Lett 24(38):11904–11912. https://doi.org/10.1021/acs.nanolett.4c03139
72. Wang M, Qiao L, Ma S, He Z (2024) Facile preparation of photothermal superhydrophobic melamine sponge decorated with MXene and lignin particles for efficient oil/water separation, fast crude oil recovery, and active deicing. Langmuir 40(11):5978–5991. https://doi.org/10.1021/acs.langmuir.3c04006

Publisher's Note Springer Nature remains neutral with regard to jurisdictional claims in published maps and institutional affiliations.